European Journal of Medicinal Chemistry 299 (2025) 118103

Contents lists available at ScienceDirect

European Journal of Medicinal Chemistry

journal homepage: www.elsevier.com/locate/ejmech

Research paper

Comparative evaluation of three ^{18}F-fluorinated FAP ligands in rodent tumor models

Chris Hoffmann [a,b], Benedikt Gröner [a,b], Victor Bahutski [a], Heike Endepols [a,b,c], Johannes Lindemeyer [d], Sven Saniternik [d], Birte Drewes [a], Marco Timmer [e], Otari Gokhadze [a], Melanie Brugger [a], Felix Neumaier [a,b], Bernd Neumaier [a,b,*], Boris D. Zlatopolskiy [a,b]

[a] Forschungszentrum Jülich GmbH, Institute of Neuroscience and Medicine, Nuclear Chemistry (INM-5), Wilhelm-Johnen-Straße, Jülich, 52428, Germany
[b] University of Cologne, Faculty of Medicine and University Hospital Cologne, Institute of Radiochemistry and Experimental Molecular Imaging, Kerpener Straße 62, 50937, Cologne, Germany
[c] University of Cologne, Faculty of Medicine and University Hospital Cologne, Department of Nuclear Medicine, Kerpener Straße 62, 50937, Cologne, Germany
[d] University of Cologne, Faculty of Medicine and University Hospital Cologne, Department of Radiology, Kerpener Straße 62, 50937, Cologne, Germany
[e] University of Cologne, Faculty of Medicine and University Hospital Cologne, Center for Neurosurgery, Kerpener Straße 62, 50937, Cologne, Germany

ARTICLE INFO

Keywords:
FAP
Fluorine-18
Positron emission tomography
Brain tumor imaging
Radiopharmaceuticals
FAPI-PET

ABSTRACT

Fibroblast activation protein (FAP) is almost exclusively expressed on cancer-associated stromal cells, making it a promising target for tumor imaging by positron emission tomography (PET). While ^{68}Ga- or Al[^{18}F]F-labeled FAP inhibitors (FAPIs) have been characterized in detail, the potential advantages of FAPIs containing a covalently bound ^{18}F-label remain largely unknown. The aim of the present work was to address this gap by comparing two FAPIs with a covalently bound ^{18}F-label and the chelator-based radioligand Al[^{18}F]F-FAPI-42.

The ^{18}F-labeled FAPIs were prepared by direct (6-[^{18}F]F-FAPI) or indirect ([^{18}F]AFA-FAPI) radiofluorination, or by the Al[^{18}F]F chelation method (Al[^{18}F]F-FAPI-42), which afforded the tracers in activity yields of 11–57 % and with molar activities of 5–170 GBq/μmol. Cellular uptake studies revealed significantly higher accumulation of all three candidates in HT1080-FAP compared to HT1080-WT cells. 6-[^{18}F]F-FAPI and Al[^{18}F]F-FAPI-42 showed comparable FAP-selectivity and tumor uptake in mice inoculated with the two cell lines and rats bearing subcutaneous DSL-6A/C1 tumors, while no *in vivo* FAP-selectivity was observed for [^{18}F]AFA-FAPI. Al[^{18}F]F-FAPI-42 exhibited lower hepatobiliary excretion and faster clearance from FAP-negative tissues in the subcutaneous tumor models. In contrast, 6-[^{18}F]F-FAPI showed higher tumor uptake and better tumor retention in an intracerebral U87 glioma tumor model. When compared to the established glioma tracer [^{18}F]FET, both FAP-targeting tracers visualized intracerebral tumors with more than two-fold higher tumor-to-background ratios.

In conclusion, while the chelator-based radioligand Al[^{18}F]F-FAPI-42 is well-suited for visualization of peripheral tumors, 6-[^{18}F]F-FAPI with a covalently bound ^{18}F-label shows more favorable properties for brain tumor imaging.

1. Background

Fibroblast activation protein (FAP) is a membrane-bound type II glycoprotein from the S9B oligopeptidase subfamily that acts as a proline-selective serine protease [1]. Expression of FAP in most normal adult tissues is low or undetectable and knockout studies suggest that it may be non-essential under physiological conditions [1,2]. However, FAP is strongly overexpressed on cancer-associated fibroblasts (CAFs) and other cells of the tumor microenvironment in the vast majority of solid tumors [1,2]. As such, radiolabeled FAP inhibitors (FAPIs) have emerged as a promising class of pantumoral positron emission tomography (PET) tracers that could be of particular value for cancers unsuitable for [^{18}F]fluorodeoxyglucose ([^{18}F]FDG) PET [3–5]. Thus, while tumor uptake of these tracers is usually similar to that of [^{18}F]FDG, lower accumulation of radiolabeled FAPIs in non-target tissues results in significantly higher tumor-to-background ratios (TBRs), especially in

* Corresponding author. Forschungszentrum Jülich GmbH, Institute of Neuroscience and Medicine, Nuclear Chemistry (INM-5), Wilhelm-Johnen-Straße, Jülich, 52428, Germany.
E-mail address: b.neumaier@fz-juelich.de (B. Neumaier).

https://doi.org/10.1016/j.ejmech.2025.118103
Received 28 July 2025; Received in revised form 25 August 2025; Accepted 26 August 2025
Available online 27 August 2025

locations with high physiological [^{18}F]FDG uptake like brain or liver [6,7].

Most radioligands for FAPI-PET imaging have been derived from small molecule inhibitors with a 4-quinolinyl-glycyl-2-cyanopyrrolidine scaffold like UAMC1110, which inhibit FAP with low nanomolar IC_{50} values and very high selectivity over related peptidases [8,9]. For example, ^{68}Ga-labeled FAPIs like [^{68}Ga]FAPI-02 [10], [^{68}Ga]FAPI-04 [11] and [^{68}Ga]FAPI-46 [12] have been developed by coupling the quinoline group in UAMC1110 or its analogs with the radiometal chelator DOTA (Fig. 1). These tracers show promising properties, such as rapid and almost complete internalization by target cells, very low accumulation in normal tissues and rapid clearance from circulation [3,10–12]. However, their practical application is limited by the relatively short half-life of gallium-68 (68 min), which prevents large-scale batch production and distribution of ^{68}Ga-labeled FAPIs via a satellite concept. In this regard, ^{18}F-labeled FAPIs provide an attractive alternative for FAPI-PET imaging, as the longer half-life of fluorine-18 (110 min) enables their centralized production and distribution to remote imaging centers. In addition to eliminating the need for on-site radiochemistry, the superior decay properties of fluorine-18 compared to gallium-68 (e.g., higher positron yield, lower positron energy) could result in an improved image quality due to higher spatial resolution [13]. Accordingly, several ^{18}F-labeled FAP-radioligands like Al[^{18}F]F-FAPI-42 [14] or Al[^{18}F]F-FAPI-74 [15] have been developed by replacement of the DOTA chelator in existing FAPIs with NOTA for radiolabeling with aluminum [^{18}F]fluoride (Al[^{18}F]F) [16] (Fig. 1). Preclinical and clinical studies with these tracers indicate that they exhibit equal or superior imaging properties when compared to ^{68}Ga-labeled radioligands with the same pharmacophore [14,15,17,18].

An alternative to chelator-based ^{18}F-labeling methods is the covalent incorporation of ^{18}F, either by direct radiofluorination or using ^{18}F-labeled prosthetic groups (PGs). For example, conjugation of an alkyne-bearing derivative of FAPI-04 with an ^{18}F-labeled glycosyl moiety has been applied to prepare the ^{18}F-fluoroglycosylated tracer candidate [^{18}F]FGlc-FAPI [19] (Fig. 1). While small-animal PET studies showed higher specific tumor uptake and retention of [^{18}F]FGlc-FAPI compared to [^{68}Ga]FAPI-04, significant hepatobiliary excretion and bone uptake of this tracer have prevented its use for tumor imaging. Likewise, FAP ligands containing a 6-[^{18}F]fluoronicotineamide moiety, such as [^{18}F]FAPI-72 and [^{18}F]FAPI-73 (Fig. 1), showed unfavorable biodistribution in preclinical studies [15]. Since parameters like molecular size, polar surface area and lipophilicity can strongly affect tissue penetration and passive transfer across the blood-brain barrier (BBB), we and others have also investigated FAPI-PET tracers obtained by direct radiofluorination of UAMC1110 derivatives to identify candidates for, e.g., brain tumor imaging. For example, SuFEx click chemistry was used to prepare the ^{18}F-fluorosulfurylated UAMC1110 analog [^{18}F]FS-FAPI (Fig. 1), but this probe showed insufficient *in vivo* stability [20]. More recently, a FAPI-PET tracer obtained by introduction of fluorine-18 at the 6-position of the quinoline ring in UAMC1110 (6-[^{18}F]F-FAPI, Fig. 1) has been evaluated in cellular assays and different preclinical tumor models [21,22]. The results demonstrated a promising FAP-selectivity of 6-[^{18}F]F-FAPI and improved tumor uptake and retention compared to [^{68}Ga]FAPI-04 in a subcutaneous tumor model [21,22]. In addition, 6-[^{18}F]F-FAPI proved to be suitable for the visualization of intracranial tumors [22], supporting clinical evidence that FAPI-PET could be applied for the detection of FAP-positive primary or metastatic cerebral lesions [23–29]. However, a direct comparison of 6-[^{18}F]F-FAPI with other ^{18}F-labeled FAPIs or non-[^{18}F]FDG radiotracers for brain tumor imaging is still lacking.

In the present work, we therefore prepared 6-[^{18}F]F-FAPI by Cu-mediated radiofluorination of the corresponding trimethylstannyl precursor and compared it with the chelator-based probe Al[^{18}F]F-FAPI-42 using cellular uptake studies and μPET imaging in different subcutaneous and intracerebral tumor models. In addition, brain tumor accumulation of both FAP-radioligands was compared with that of the established glioma tracer *O*-(2-[^{18}F]fluoroethyl)-L-tyrosine ([^{18}F]FET) and the *in vivo* FAP-specificity of 6-[^{18}F]F-FAPI was studied by blocking and displacement studies. Finally, the hitherto unknown FAP-radioligand 6-{[^{18}F]fluoro-2-(methylamino)nicotinamido}propoxy-UAMC1110 ([^{18}F]AFA-FAPI, Fig. 1) was prepared by indirect radiofluorination of appropriately modified UAMC1110 with an amine-reactive PG and evaluated with regard to its *in vitro* and *in vivo* FAP-selectivity.

2. Results

2.1. Synthesis of radiolabeling precursors and non-radioactive reference compounds

2.1.1. Preparation of radiolabeling precursor **5**

The trimethylstannyl precursor **5** was obtained as follows (Scheme

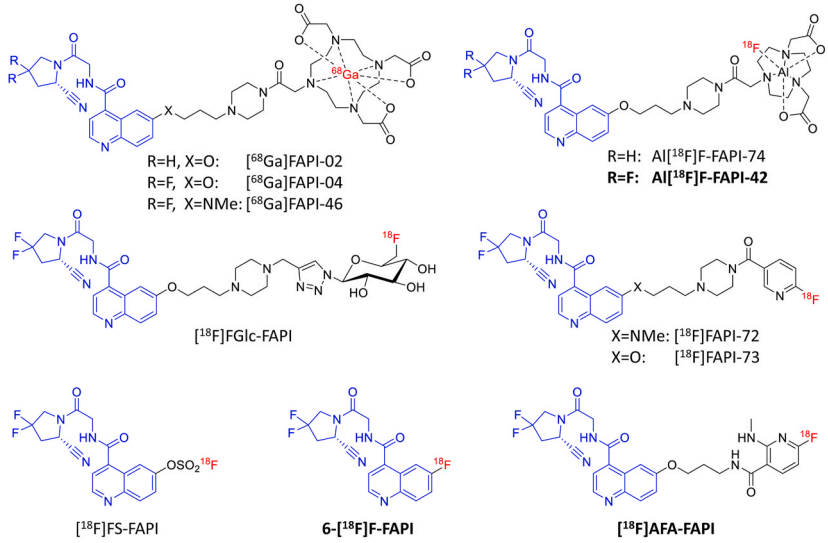

Fig. 1. Selected examples of ^{68}Ga- and ^{18}F-labeled FAP inhibitors (FAPIs) for PET imaging, with the common 4-quinolinyl-glycyl-2-cyanopyrrolidine pharmacophore highlighted in blue. Bold names indicate compounds prepared and evaluated in the present study. (For interpretation of the references to color in this figure legend, the reader is referred to the Web version of this article.)

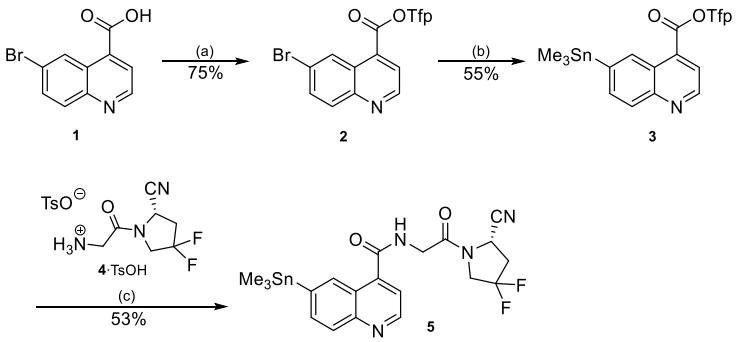

Scheme 1. Preparation of trimethylstannyl radiolabeling precursor **5**. Conditions: (a) 2,3,5,6-tetrafluorophenol, EDC•HCl, DCM, rt, 16 h. (b) $Pd(Ph_3P)_4$, LiCl, Sn_2Me_6, toluene, 120 °C, 3 h. (c) Et_3N, DCM, rt, 3 h. Abbreviations: TsO^- – tosylate, Tfp – 2,3,5,6-tetrafluorophenyl.

1). Active ester **2**, which was prepared by esterification of the corresponding carboxylic acid (**1**) with 2,3,5,6-tetrafluorophenol, was subjected to Pd-catalyzed stannylation with Sn_2Me_6 to afford 2,3,5,6-tetrafluorophenyl 6-(trimethylstannyl)-quinoline-4-carboxylate (**3**). Subsequent coupling of **3** with glycine amide **4**•TsOH [30] afforded radiolabeling precursor **5** in a total yield of 22 % over the three steps. The corresponding pinacol boronate precursor **6** was prepared according to the literature [20].

Notably, alternative synthetic approaches employing the respective carboxylic acids with EDC/HOBt or HATU coupling protocols, instead of the OTfp active ester route, yielded the radiolabeling precursor **5** (and 6-F-FAPI, see preparation below) in lower overall yields. In addition, purification of the products obtained by these direct coupling methods proved to be considerably more challenging.

2.1.2. Preparation of aminopropyl-functionalized UAMC1110 derivative *12*

Aminopropyl-functionalized UAMC1110 (**12**) was prepared from 6-(3-chloropropoxy)quinoline-4-carboxylic acid (**7**) [31] (Scheme 2). To this end, **7** was converted to the corresponding azide **8**, which was esterified with 2,3,5,6-tetrafluorophenol to obtain the active ester **9**. Subsequent coupling of **9** with **4**•TsOH afforded azide-substituted amide **10**, which was hydrogenated over Pd/C in the presence of Boc_2O to give the *N*-Boc protected intermediate **11**. Finally, acidic deprotection of **11** in the presence of triisopropylsilane as *tert*-butyl cation scavenger afforded the desired aminopropyl-functionalized UAMC1110 derivative **12**•TFA in a total yield of 56 % over five steps.

2.1.3. Preparation of 6-F-FAPI

The non-radioactive reference compound (*S*)–*N*-[2-(2-cyanopyrrolidin-1-yl)-2-oxoethyl]-6-fluoroquinoline-4-carboxamide (6-F-FAPI) was obtained starting from 6-fluoroquinoline-2,4-dicarboxylic acid (**14**), which was prepared from 5-fluoroindoline-2,3-dione (**13**) according to the literature [8] (Scheme 3). After decarboxylation of **14**, the resulting monocarboxylic acid **15** was esterified with 2,3,5,6-tetrafluorphenol to give the bench-stable OTfp-ester **16**. Subsequent reaction of **16** with **4**•TFA afforded 6-F-FAPI in 15 % yield over three steps.

2.1.4. Preparation of AFA-FAPI

The reference compound AFA-FAPI was synthesized as follows (Scheme 4). 6-Fluoro-2-(methylamino)nicotinic acid (**17**) [32] was transformed into the respective acid chloride, which was directly conjugated with amine **12** to give AFA-FAPI in 48 % yield over two steps.

2.2. Radiotracer syntheses

2.2.1. Preparation of Al[^{18}F]F-FAPI-42

The radiosynthesis of Al[^{18}F]F-FAPI-42 was performed according to the literature [33].

2.2.2. Preparation of 6-[^{18}F]F-FAPI by Cu-mediated radiofluorination

The radiosynthesis of 6-[^{18}F]F-FAPI was initially attempted using the

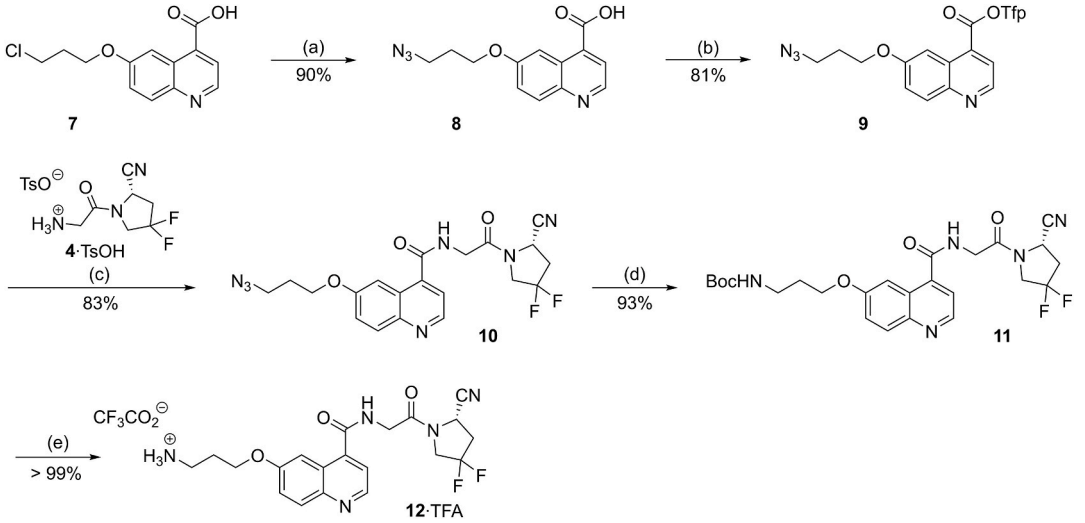

Scheme 2. Synthesis of the aminopropyl-functionalized UAMC1110 derivative **12**•TFA. Conditions: (a) NaN_3, NaI, DMF, 2,6-lutidine, 60 °C, 24 h. (b) 2,3,5,6-tetrafluorophenol, EDC, DCM, rt, 72 h. (c) Et_3N, DCM, rt, 24 h. (d) H_2, 10 % Pd/C, Boc_2O, EtOAc, MeCN, rt, 3.5 h. (e) TFA, triisopropylsilane, H_2O (95:2.5:2.5), rt, 15 min. Abbreviations: rt – room temperature, TsO^- – tosylate, Tfp – 2,3,5,6-tetrafluorophenyl, TFA – trifluoroacetate.

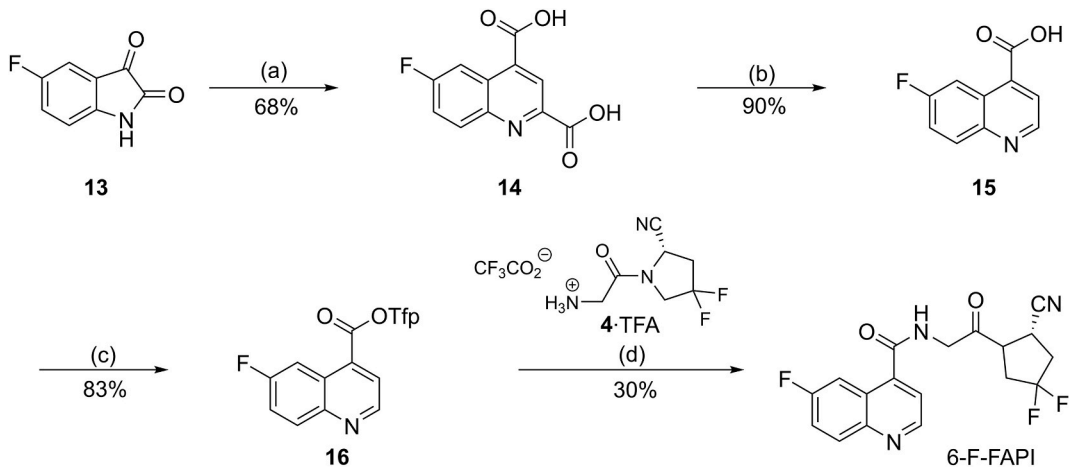

Scheme 3. Synthesis of 6-F-FAPI. Conditions: (a) sodium pyruvate, 6 M NaOH, 130 °C, 4 h. (b) $PhNO_2$, 210 °C, 50 min. (c) 2,3,5,6-tetrafluorophenol, EDC, CH_2Cl_2, rt, 16 h. (d) DIPEA, CH_2Cl_2, rt, 6 h. Abbreviations: TFA – trifluoroacetate, Tfp – 2,3,5,6-tetrafluorophenyl.

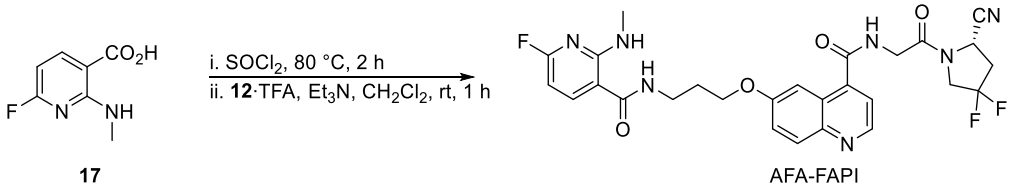

Scheme 4. Synthesis of AFA-FAPI. Conditions: i. $SOCl_2$, 80 °C, 2 h, ii. **12**•TFA, Et_3N, CH_2Cl_2, rt, 1 h.

boronic acid precursor **6**. However, despite extensive optimization of the reaction conditions, radiochemical conversions (RCCs) using this precursor did not exceed 17 % (see supporting information for further details). The radiotracer was therefore prepared from the stannyl precursor **5**, using the optimized protocol for radiofluorination of stannyl precursors developed in our group [34] (Scheme 5).

To this end, [^{18}F]fluoride ([^{18}F]F^-) was eluted from a QMA cartridge with a solution of Et_4NOTf (1 mg, 4 μmol) in MeOH (500 μL), and the MeOH was evaporated at 80 °C under reduced pressure in a stream of argon. The residue was taken up in a solution of Cu(4-PhPy)$_4$(ClO$_4$)$_2$ and precursor **5** (10 μmol of each) in DMI (800 μL), and the reaction mixture was heated at 90 °C for 10 min to afford crude 6-[^{18}F]F-FAPI with RCCs of 48 ± 11 % (n = 6). The reaction mixture was diluted with H_2O (15 mL) and the crude product was trapped on a reversed-phase cartridge, washed with H_2O (5 mL) and eluted with MeCN (500 μL). Following dilution with H_2O (1 mL) and purification by preparative HPLC, 6-[^{18}F]F-FAPI was obtained in activity yields (AYs) of 19 ± 2 % (n = 6) and radiochemical purities (RCPs) of ≥99 %. The molar activity (A_m) of the tracer amounted to 71 GBq/μmol for 1.1 GBq 6-[^{18}F]F-FAPI (from 5.9 GBq [^{18}F]F^-).

2.2.3. Preparation of [^{18}F]AFA-FAPI by indirect radiofluorination

The radiosynthesis of [^{18}F]AFA-FAPI was performed according to a protocol for indirect radiofluorination with amine-reactive 1-alkylamino-7-[^{18}F]fluoro-8-azaisatoic anhydrides ([^{18}F]AFAs) [32] (Scheme 6). For preparation of the respective [^{18}F]AFA, [^{18}F]F^- was loaded onto an anion exchange-cartridge and slowly eluted with a solution of precursor **18**•TfOH (31 μmol) in MeCN/*t*BuOH (1 mL, 1:2 v/v), which afforded, after purification by solid phase extraction (SPE), a solution of [^{18}F]**19** in MeCN. After evaporation of the solvent at 85 °C under reduced pressure in a stream of argon, a solution of **12**•TFA (10 μmol) in 0.2 M borate buffer (pH 8.7)/MeCN (500 μL) was added and the mixture was heated at 35 °C for 15 min. The crude [^{18}F]AFA-FAPI thus obtained was purified by preparative HPLC and formulated as an injectable solution. [^{18}F]AFA-FAPI was obtained in AYs of 13 ± 5 % (n = 4) and RCPs of >97 % within a total preparation time of 100 min. The A_m amounted to 170 GBq/μmol for 770 MBq [^{18}F]AFA-FAPI (from 3.5 GBq [^{18}F]F^-).

2.3. Biological evaluation

2.3.1. Cellular uptake studies

Cellular uptake studies with the radiotracers were carried out in FAP-transfected (HT1080-FAP) and non-transfected (HT1080-WT) human fibrosarcoma cells. As summarized in Fig. 2, all three tracers showed significantly higher uptake by HT1080-FAP compared to HT1080-WT cells, although absolute cellular uptake as well as the degree of FAP-

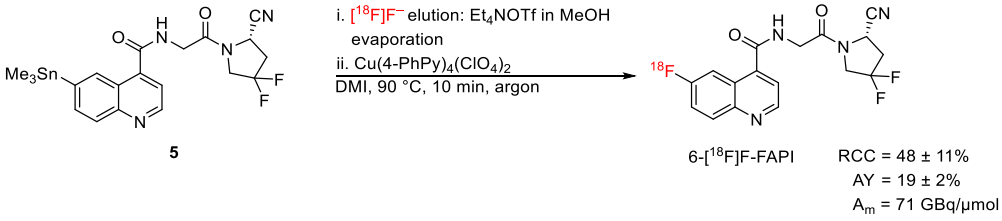

Scheme 5. Preparation of 6-[^{18}F]F-FAPI by the NextGen protocol for Cu-mediated radiofluorination. Conditions: Elution of [^{18}F]F^- with Et_4NOTf (1 mg, 4 μmol) in MeOH (500 μL) followed by concentration at 80 °C under reduced pressure in a stream of argon within 3 min; the residue was taken up in a solution of Cu(4-PhPy)$_4$(ClO$_4$)$_2$ and **5** (10 μmol of each) in DMI (800 μL) and the mixture was heated at 90 °C for 10 min under argon.

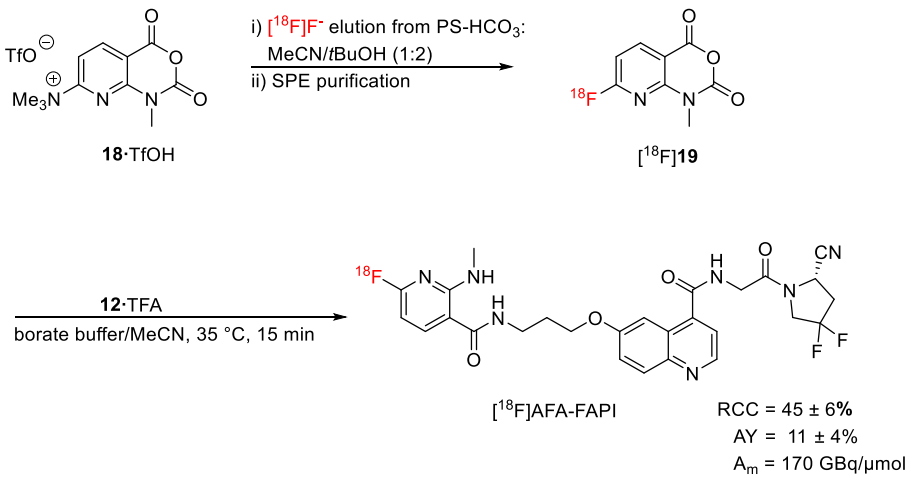

Scheme 6. Radiosynthesis of [^{18}F]AFA-FAPI by indirect radiofluorination. Conditions: Elution of [^{18}F]F$^-$ with **18**•TfOH (12 mg, 31 µmol) in MeCN/*t*BuOH (1.2 mL, 1:2 v/v) followed by SPE and evaporation at 85 °C under reduced pressure in a stream of argon; the resulting [^{18}F]**19** was taken up in a solution of **12**•TFA (5.3 mg, 10 µmol) in 0.2 M borate buffer (pH 8.7)/MeCN (500 µL, 9:1) and the mixture was heated at 35 °C for 15 min. Abbreviations: TfO$^-$ – trifluoromethanesulfonate, TFA – trifluoroacetate, SPE – solid phase extraction.

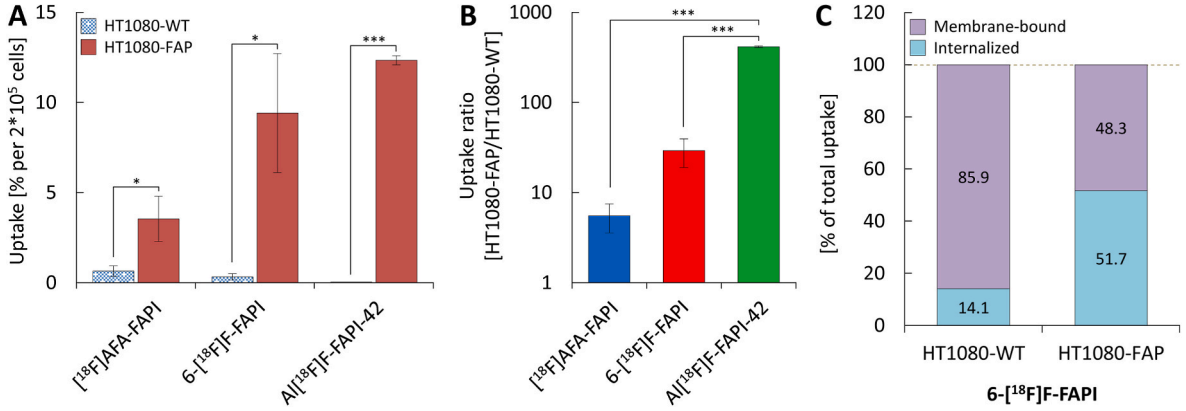

Fig. 2. *In vitro* uptake of FAP-radioligands by wild type (HT1080-WT) and FAP-transfected (HT1080-FAP) human fibrosarcoma cells. (A) Comparison of absolute cellular uptake by HT1080-WT and HT1080-FAP cells quantified after incubation with the different probes for 60 min and expressed as the percentage of total activity added per 2 × 10^5 cells (n = 3–4 per tracer). (B) FAP-selectivity of the probes determined as the ratio between cellular uptake by HT1080-FAP and HT1080-WT cells after 60 min (same data as in A). Note that the y-axis is shown on a log scale to facilitate comparison of the uptake ratios for the different probes. (C) Comparison of membrane-bound and internalized radioactivity after incubation of cells with 6-[^{18}F]F-FAPI for 60 min (n = 1). Statistically significant differences between the groups in A and B were identified by two-tailed t-tests (A) or Welch's ANOVA with Games-Howell post-hoc test (B), respectively, and are indicated by asterisks (*, $p < 0.05$, ***, $p < 0.001$).

selectivity were variable. Thus, compared to the other tracers, [^{18}F]AFA-FAPI exhibited the highest uptake by HT1080-WT cells (0.64 ± 0.30 %) and the lowest uptake by HT1080-FAP cells (3.54 ± 1.26 %) (Fig. 2A), which resulted in a relatively low FAP/WT accumulation ratio of 5 ± 2 (Fig. 2B). 6-[^{18}F]F-FAPI showed roughly two-fold lower uptake by HT1080-WT cells (0.3 ± 0.2 %) and three-fold higher uptake by HT1080-FAP cells (9.4 ± 3.3 %), as reflected in a six-fold higher FAP/WT ratio of 29 ± 10 (Fig. 2B). Finally, Al[^{18}F]F-FAPI-42 showed almost no uptake by HT1080-WT cells (0.03 ± 0.01 %) and the highest uptake by HT1080-FAP cells (12.34 ± 0.25 %), so that the FAP/WT ratio for this probe amounted to 414 ± 8 and was significantly higher than that for the two other probes (Fig. 2B). Separation of the membrane-bound and cytoplasmic radioactivity fractions after incubation of cells with 6-[^{18}F]F-FAPI demonstrated that approximately half of the cell-associated radioactivity in HT1080-FAP cells was internalized, while most of the cell-associated radioactivity in HT1080-WT cells (>85 %) was membrane-bound (Fig. 2C).

2.3.2. *PET imaging in a subcutaneous HT1080 xenograft mouse model*

Next, the biodistribution of the three FAP-radioligands was evaluated in mice bearing subcutaneous HT1080-FAP or HT1080-WT tumors. As illustrated in Fig. 3A and B, both Al[^{18}F]F-FAPI-42 and 6-[^{18}F]F-FAPI showed pronounced accumulation in the FAP-positive HT1080-FAP tumors and very little washout. The uptake of Al[^{18}F]F-FAPI-42 peaked at 20 min p.i. (SUV_{bw} of 61), while 6-[^{18}F]F-FAPI reached a plateau of high mean uptake values between 32 and 68 min p.i. (SUV_{bw} values of 76–78) (Fig. 3B). When uptake was summed over four consecutive 30 min periods, both tracers showed highest cumulative uptake into FAP-positive tumors at 30−60 min p.i. and less than 15 % washout during the remaining time periods (Table 1). In contrast, uptake of [^{18}F]AFA-FAPI by FAP-positive tumors already peaked at about 10 min p.i (Fig. 3A and B). and highest cumulative uptake was observed for the period 0−30 min p.i., which was followed by a rapid washout to less than 30 % of the initial value at 90−120 min p.i. (Table 1).

For both Al[^{18}F]F-FAPI-42 and 6-[^{18}F]F-FAPI, uptake into HT1080-FAP tumors after the initial 30 min was significantly higher than uptake into FAP-negative HT1080-WT tumors. The uptake ratio (HT1080-FAP/HT1080-WT) was higher for 6-[^{18}F]F-FAPI during the first hour p.i., and higher for Al[^{18}F]F-FAPI-42 during the second hour p.i. (Table 1).

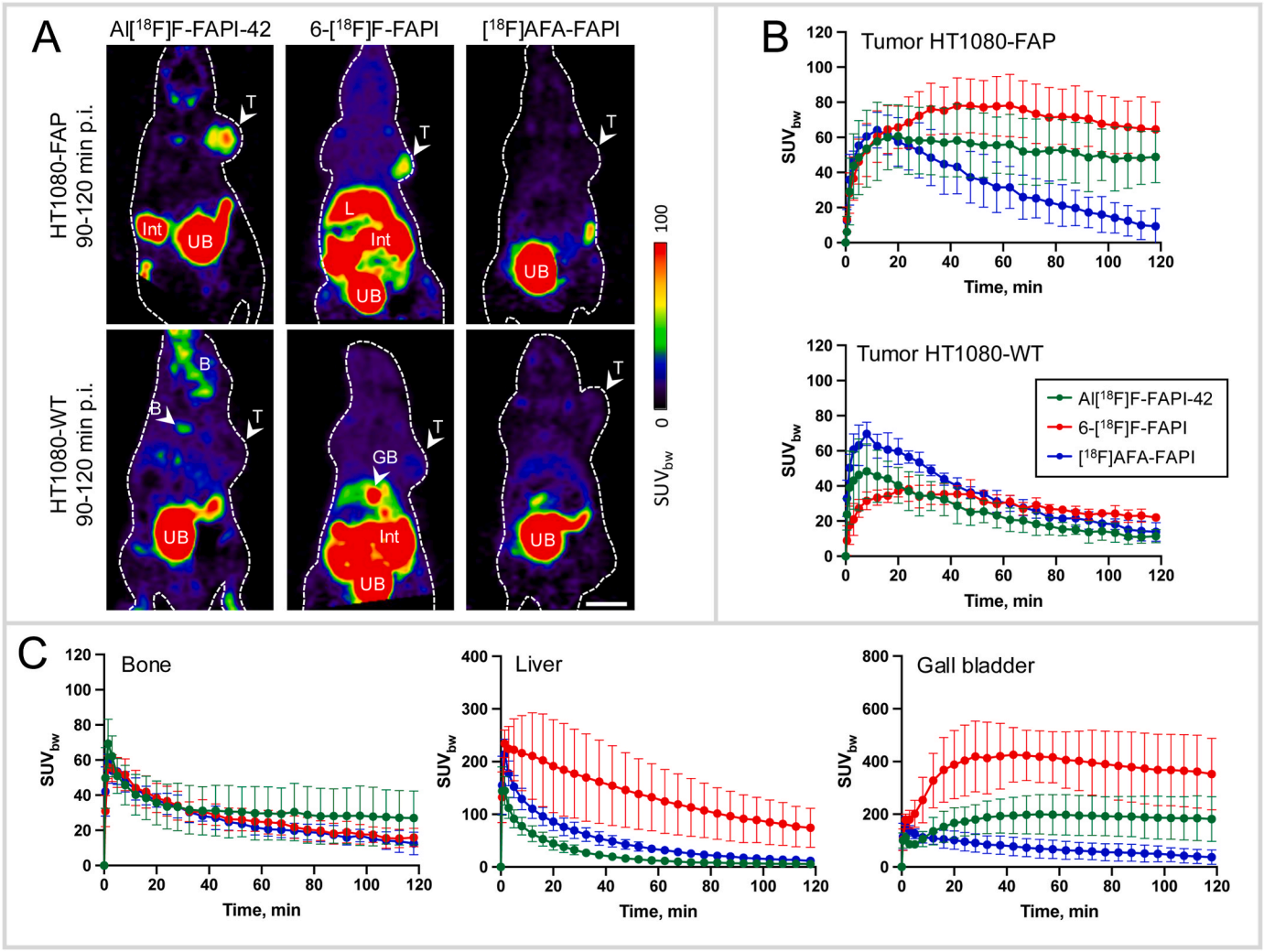

Fig. 3. Comparison of radiolabeled FAP ligands in a subcutaneous HT1080 xenograft model. (A) Representative summed PET images (horizontal sections) of mice implanted with FAP-positive HT1080-FAP (top row) or FAP-negative HT1080-WT (bottom row) tumors for the uptake period 90–120 min p.i. The dashed line indicates the mouse outline, while the arrows indicate the location of the subcutaneous tumors. (B) Time-activity-curves (mean ± standard deviation) for the different tracers in HT1080-FAP (top row) or HT1080-WT (bottom row) tumors. (C) Time-activity-curves for the different tracers in bone, liver and gall bladder. n = 3–5 per tracer, see Table 1. Scale bar in A: 10 mm. Abbreviations: B – bone, GB – gall bladder, Int – intestine, L – liver, T – tumor, UB – urinary bladder.

Although 6-[^{18}F]F-FAPI showed a higher mean uptake into HT1080-FAP tumors than Al[^{18}F]F-FAPI-42 (Fig. 3B), the TBR of the former tracer was lower. Thus, due to fast washout from FAP-negative tissues (Suppl. Fig. S9 [background] B), very high TBRs of 12–14 were achieved with Al[^{18}F]F-FAPI-42 at 60–120 min p.i. Washout of 6-[^{18}F]F-FAPI from FAP-negative tissues was slower and the TBRs for this tracer did not exceed 5. However, they showed a steady increase during the 120 min measurement period as well. For [^{18}F]AFA-FAPI, there was no difference in tracer uptake between FAP-positive and FAP-negative tumors, and the time-activity curves (TACs) for both tumors (Fig. 3B) closely resembled the background TAC for 6-[^{18}F]F-FAPI (i.e. high initial uptake followed by washout).

All three tracers were eliminated by renal and hepatobiliary excretion. Accumulation in the gall bladder and intestine was highest for 6-[^{18}F]F-FAPI followed by Al[^{18}F]F-FAPI-42 (Fig. 3C). [^{18}F]AFA-FAPI showed the lowest biliary excretion. Retention in the liver was highest for 6-[^{18}F]F-FAPI (Fig. 3C). The distribution ($t_{1/2,fast}$) and elimination ($t_{1/2,slow}$) half-lives determined from plasma clearance curves (Suppl. Fig. S10) amounted to 1.7 and 15 min for Al[^{18}F]F-FAPI-42, 1.5 and 57 min for 6-[^{18}F]F-FAPI, and 2.4 and 29 min for [^{18}F]AFA-FAPI (Suppl. Table S4).

2.3.3. PET imaging in a subcutaneous DSL allograft rat model

The performance of 6-[^{18}F]F-FAPI was further compared with that of Al[^{18}F]F-FAPI-42 in rats bearing subcutaneous DSL-6A/C1 tumors, a model with physiological FAP expression in stromal CAFs [35,36]. Compared to the HT1080-FAP tumors in the mouse model, both tracers showed more than two-fold higher absolute tumor uptake in this rat model (Fig. 4A). However, as already observed in the mouse model, the tumoral TACs for both tracers were almost identical and washout of 6-[^{18}F]F-FAPI from FAP-negative tissues was slower, leading to considerably higher TBRs for Al[^{18}F]F-FAPI-42 (Fig. 4B).

2.3.4. PET imaging in an orthotopic U87 glioma xenograft rat model

As previous pilot studies with [^{68}Ga]FAPI-02 and -04 have yielded promising results in glioblastoma patients [23,24], we also compared 6-[^{18}F]F-FAPI and Al[^{18}F]F-FAPI-42 with the established amino acid tracer [^{18}F]FET [37,38] in an orthotopic glioma rat model (Fig. 5). Although [^{18}F]FET showed higher absolute tumor uptake, the two FAP-targeting tracers exhibited much lower background uptake in healthy brain tissue (Fig. 5A), which resulted in higher TBRs for both 6-[^{18}F]F-FAPI and Al[^{18}F]F-FAPI-42 compared to [^{18}F]FET (Fig. 5B). In addition, while accumulation of 6-[^{18}F]F-FAPI and Al[^{18}F]F-FAPI-42 was restricted to the T2-delineated lesion and most pronounced in the

Table 1
Comparison of tracer uptake by subcutaneous FAP-positive (HT1080-FAP) and FAP-negative (HT1080-WT) tumors in mice.

Tracer	SUV_{bw} HT1080-FAP	SUV_{bw} HT1080-WT	Ratio	Significance[a]
Al[^{18}F]F-FAPI-42	(n = 4)	(n = 5)		F(1,7) = 11.2; p = 0.0123
0–30 min	47.6 ± 18.6	40.2 ± 14.0	1.2	p = 0.8758
30–60 min	56.9 ± 19.0	28.2 ± 8.1	2.0	p = 0.0108
60–90 min	52.7 ± 18.0	17.9 ± 5.3	3.0	p = 0.0017
90–120 min	48.6 ± 16.6	12.5 ± 4.7	3.9	p = 0.0011
6-[^{18}F]F-FAPI	(n = 5)	(n = 3)		F(1,6) = 25.8; p = 0.0023
0–30 min	50.9 ± 12.8	28.3 ± 6.4	1.8	p = 0.0776
30–60 min	77.0 ± 15.3	33.7 ± 6.0	2.3	p = 0.0003
60–90 min	73.7 ± 16.9	27.6 ± 3.1	2.7	p = 0.0001
90–120 min	66.8 ± 16.0	23.4 ± 3.0	3.0	p = 0.0003
[^{18}F]AFA-FAPI	(n = 4)	(n = 4)		F(1,6) = 0.27; p = 0.6198
0–30 min	50.1 ± 10.2	57.0 ± 7.8	0.9	n.s.
30–60 min	40.1 ± 15.4	39.3 ± 3.6	1.0	n.s.
60–90 min	24.4 ± 11.6	24.8 ± 4.0	1.0	n.s.
90–120 min	13.2 ± 9.1	16.8 ± 4.8	0.8	n.s.

[a] Shown are results of two-way ANOVA, factor "tumor type".

core of the tumor, [^{18}F]FET showed a more diffuse accumulation pattern that appeared to partly extend into the peritumoral brain zone (Fig. 5A). When comparing the two FAP-targeting tracers, absolute tumor uptake was higher and more persistent for 6-[^{18}F]F-FAPI. Moreover, and in contrast to the results in the subcutaneous DSL model, there was no significant difference between the TBRs for 6-[^{18}F]F-FAPI and Al[^{18}F]F-FAPI-42 (Fig. 5B).

Finally, since contrast-enhanced MRI (Fig. 6A, T1+CA) indicated extensive BBB disruption within the T2-delineated lesion (Fig. 6A, T2), we performed blocking and displacement experiments to confirm that accumulation of 6-[^{18}F]F-FAPI in the intracerebral tumors was due to FAP-specific binding. As illustrated in Fig. 6A, co-injection of 6-[^{18}F]F-FAPI with an excess of the FAP-selective ligand UAMC1110 (5 mg/kg) reduced tumoral tracer uptake by approximately 70 %. Likewise, administration of UAMC1110 (5 mg/kg) 60 min after tracer injection produced a rapid decrease of tumoral tracer accumulation by approximately 50 % within 20 min and 68 % within 60 min (Fig. 6B).

3. Discussion

Although a number of chelator-based ^{68}Ga- or Al[^{18}F]F-labeled FAP-radioligands derived from UAMC1110 or related compounds have been described, there is still a lack of comparative biological data, especially for tracers bearing a covalently bound ^{18}F-label. Since such compounds could have pharmacokinetic advantages and a more favorable biodistribution profile for certain applications (e.g., brain tumor imaging), the present study focused on two ^{18}F-labeled UAMC1110 derivatives prepared by direct or indirect radiofluorination and their comparison with Al[^{18}F]F-FAPI-42 as a chelator-based reference tracer. Under optimized conditions, the two covalently labeled radiotracer candidates could be prepared in AYs of 11–57 % and with molar activities of 5–170 GBq/μmol using either Cu-mediated radiofluorination of the corresponding trimethylstannyl precursor with a NextGen Cu mediator (6-[^{18}F]F-FAPI), or indirect radiofluorination of aminopropyl-functionalized UAMC1110 with an amine-reactive [^{18}F]AFA PG ([^{18}F]

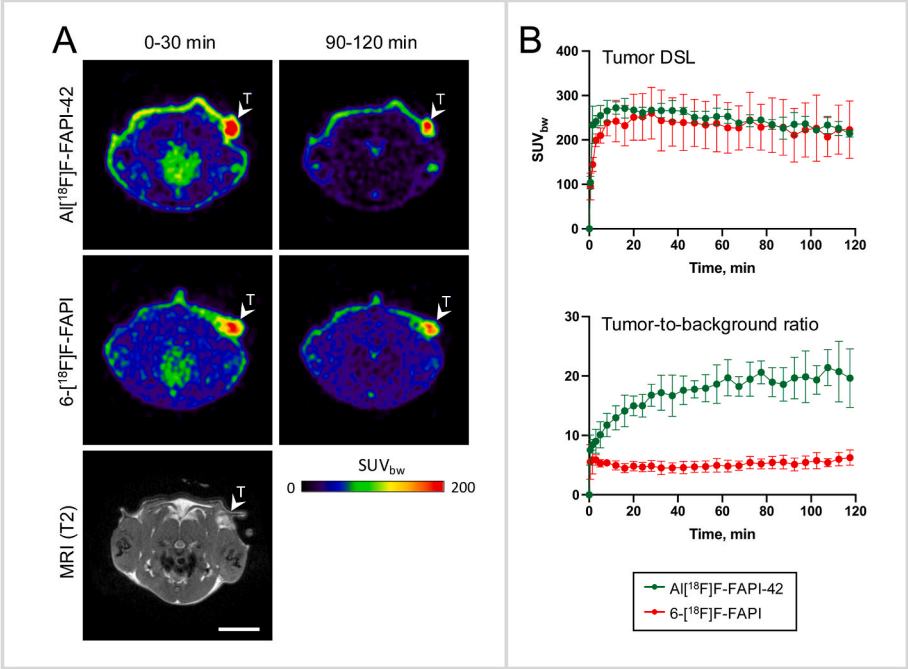

Fig. 4. Comparison of Al[^{18}F]F-FAPI-42 and 6-[^{18}F]F-FAPI in a subcutaneous DSL-6A/C1 allograft model. (A) Representative summed PET images (transverse sections) obtained with the two tracers in the same rat (measured on different days) for the uptake periods 0–30 min p.i. and 90–120 min p.i. (B) Time-activity-curves for the tumor (top) and changes in the tumor-to-background ratio over time (bottom). n = 4 per tracer. Scale bar in A: 15 mm. Abbreviation: T – tumor.

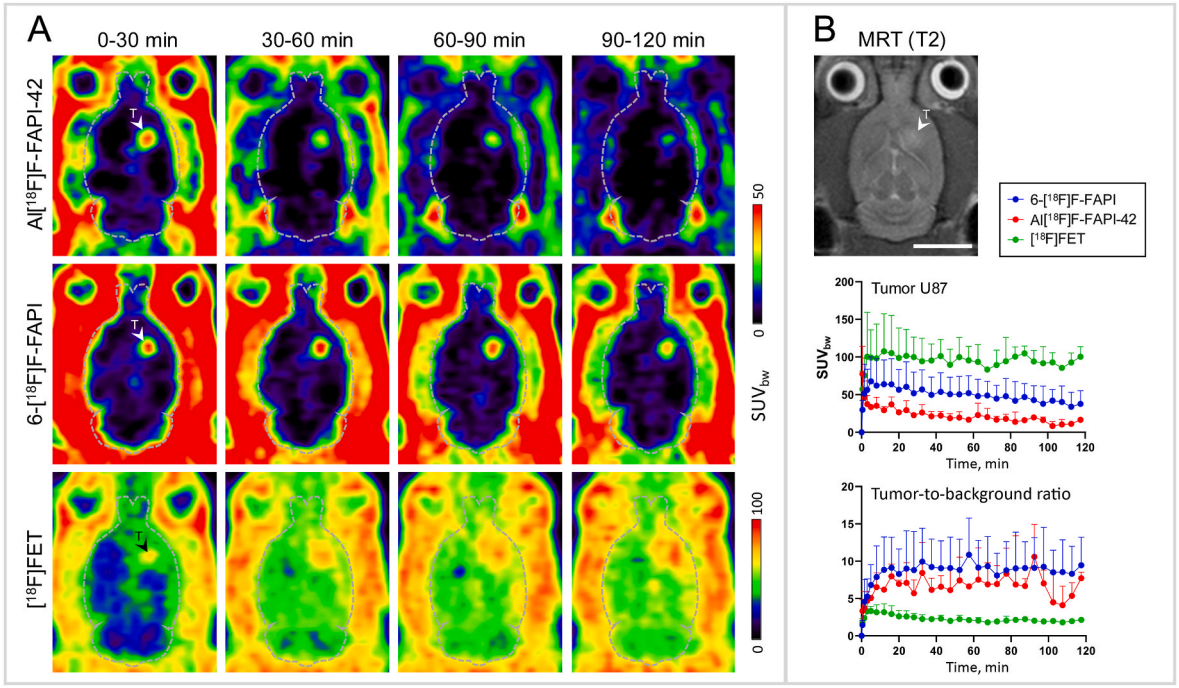

Fig. 5. Comparison of Al[^{18}F]F-FAPI-42, 6-[^{18}F]F-FAPI and [^{18}F]FET in an orthotopic U87 glioma rat model. (A) Representative summed PET images (horizontal sections) for the indicated uptake periods obtained in the same rat with the three tracers. (B) T2-weighted MRI of the same rat, showing the location of the intracerebral tumor (top). Also shown are time activity curves (n = 3 per tracer) for the tumor (middle) and changes in the tumor-to-background ratio (n = 3) over time (bottom). Scale bar in B: 10 mm. Abbreviation: T - tumor.

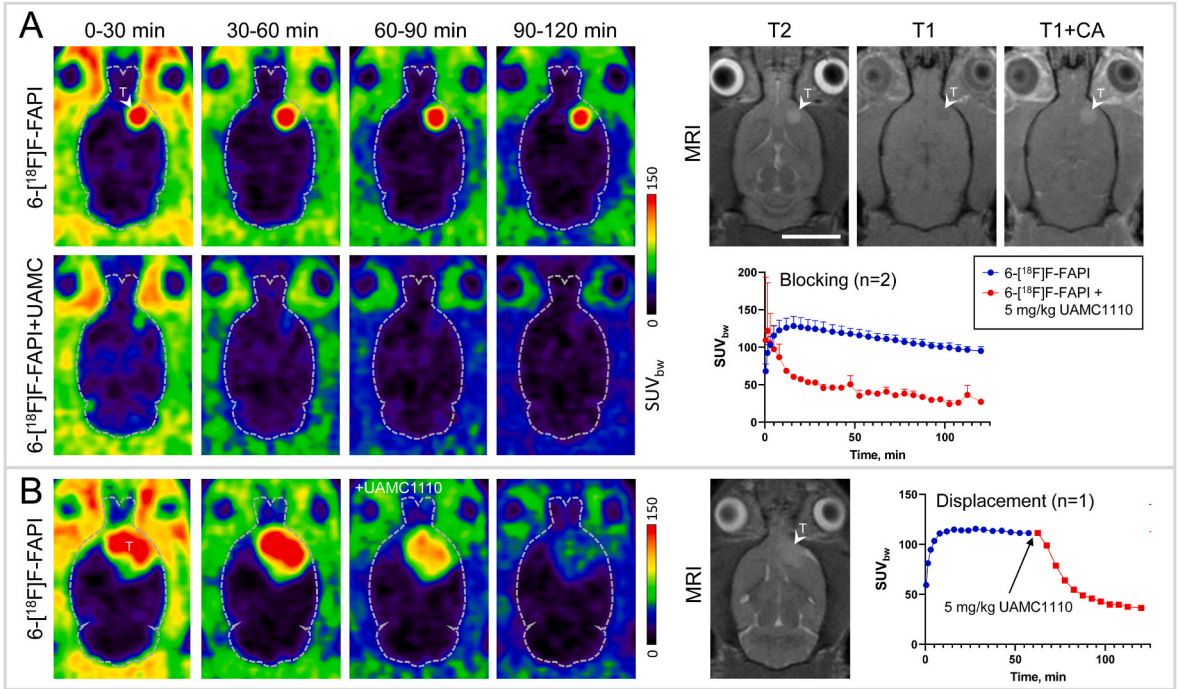

Fig. 6. Blocking and displacement of 6-[^{18}F]F-FAPI accumulation in the orthotopic U87 glioma rat model. (A) Representative summed PET images (horizontal sections) for the indicated uptake periods obtained in the same rat without (upper row) and with (lower row) co-injection of 5 mg/kg UAMC1110. Also shown on the right are T2-weighted (left), T1-weighted (middle) and contrast-enhanced T1-weigthed (right) MRI images of the same rat and mean time-activity-curves for the tumor (n = 2). (B) Summed PET images and corresponding T2-weigthed MRI of a rat injected with UAMC1110 (5 mg/kg) 60 min after tracer injection. Also shown is the time-activity-curve for the tumor (n = 1). Scale bar in A: 10 mm. Abbreviations: CA - contrast agent, T - tumor.

AFA-FAPI), respectively.

A first analysis of the *in vitro* properties with human fibrosarcoma cells revealed significantly higher uptake of all three radiotracers into FAP-transfected (HT1080-FAP) compared to wild type (HT1080-WT) cells. However, absolute uptake of the probes by HT1080-FAP cells as well as their exact FAP-selectivity showed considerable differences, with

[^{18}F]AFA-FAPI exhibiting the poorest and Al[^{18}F]F-FAPI-42 the best *in vitro* performance.

In vivo PET imaging in mice bearing subcutaneous HT1080-FAP or HT1080-WT tumors demonstrated a lack of FAP-specific tumor accumulation for [^{18}F]AFA-FAPI. Comparable results have previously been reported for structurally similar FAP-radioligands labeled with a 6-[^{18}F]fluoronicotineamide moiety [15], suggesting that such UAMC1110 derivatives are not suitable as FAP-selective PET tracers.

In contrast, 6-[^{18}F]F-FAPI exhibited a promising *in vivo* FAP-specificity in the subcutaneous HT1080 tumor model, as reflected in significantly higher uptake by FAP-expressing compared to WT tumors. In addition, 6-[^{18}F]F-FAPI showed good tumor retention and low uptake by FAP-negative background tissues, resulting in TBRs of around 5 in both, mice bearing subcutaneous HT1080-FAP tumors and rats bearing subcutaneous DSL-6A/C1 tumors. However, while absolute tumor uptake of 6-[^{18}F]F-FAPI in the subcutaneous tumor models was comparable to or even somewhat higher than that of Al[^{18}F]F-FAPI-42, the latter showed faster washout from FAP-negative background tissues, so that much higher TBRs (up to 20) were achieved with this radioligand. Additionally, 6-[^{18}F]F-FAPI exhibited more pronounced hepatobiliary excretion, which could hamper its use for detection of abdominal tumors. Taken together, these findings confirm and extend the results of previous studies with 6-[^{18}F]F-FAPI, which observed tumor-to-muscle ratios of 4–8 in different subcutaneous tumor models and predominant hepatobiliary excretion of the radiotracer [21,22]. In addition, the direct comparison of 6-[^{18}F]F-FAPI with Al[^{18}F]F-FAPI-42 performed in the present work demonstrates that the latter tracer is superior for high-contrast visualization of peripheral tumors, at least in preclinical models. However, it should be noted that the more favorable hepatobiliary clearance of Al[^{18}F]F-FAPI-42 observed in our models may not necessarily translate to tumors located in organs with complex physiology such as the liver or pancreas, where background signal could be influenced by local tracer uptake or metabolism.

Apart from its usefulness for imaging peripheral tumors, FAPI-PET represents a promising approach for the detection and staging of brain tumors like gliomas. Thus, brain tumor imaging with the standard-of-care radiotracer [^{18}F]FDG is often hampered by high physiological tracer uptake in the brain, and several recent case reports and pilot studies indicate that FAPI-PET imaging may be superior in detecting small primary or metastatic cerebral lesions [23–29]. In addition, 6-[^{18}F]F-FAPI has been successfully used to visualize intracranial tumors in an orthotopic tumor model [22], but a direct comparison with other ^{18}F-labeled FAPIs or non-[^{18}F]FDG radiotracers for brain tumor imaging was so far still lacking. As such, the present study also compared the imaging properties of 6-[^{18}F]F-FAPI and Al[^{18}F]F-FAPI-42 with that of the established brain tumor tracer [^{18}F]FET in an orthotopic U87 glioma model. The fact that both FAP-radioligands showed tumor-specific accumulation in this model is consistent with previous results demonstrating that U87 cells recruit a large number of FAP-positive murine stromal cells and/or exhibit upregulated FAP-expression *in vivo* [23,39]. Moreover, even though absolute tumor uptake of the FAP-radioligands was lower than that of [^{18}F]FET, they exhibited more than two-fold higher TBRs due to much lower uptake by healthy brain tissue. Interestingly, while the TBRs for Al[^{18}F]F-FAPI-42 in the orthotopic glioma model were roughly half of those achieved in the subcutaneous models, the TBRs for 6-[^{18}F]F-FAPI in the orthotopic model were two-fold higher, which resulted in comparable TBRs for both tracers in the brain tumor model. In addition, 6-[^{18}F]F-FAPI showed higher absolute tumor uptake and a better tumor retention than Al[^{18}F]F-FAPI-42, suggesting that it may represent a superior candidate for brain tumor imaging. This could at least in part be related to the lack of a chelator, improving tissue- and brain-penetration through increased lipophilicity and reduced molecular size of the probe. Although brain tumors often compromise the integrity of the BBB, there can be significant regional heterogeneity and interindividual differences in the degree of BBB-disruption [40,41]. Accordingly, FAP-radioligands capable of penetrating into tumors or tumor regions with intact BBB would be preferable, but the hydrophilic nature of the chelators in ^{68}Ga- or Al[^{18}F]F-labeled tracers and their considerable molecular size are expected to result in negligible passive transfer across the BBB [42]. Indeed, tumoral tracer accumulation in previous studies with ^{68}Ga-labeled FAP-radioligands was exclusively observed in contrast-enhancing gliomas [23,43] suggesting that brain uptake of chelator-based radioligands in patients with an intact BBB may be insufficient. Moreover, and in line with our present findings, a recent preclinical study showed that uptake of [^{68}Ga]FAPI-04 into intracerebral U87 tumors is much lower than that of the ^{11}C-labeled probe [^{11}C]RJ1102, which closely resembles 6-[^{18}F]F-FAPI but contains an [^{11}C]methoxy instead of the [^{18}F]fluorine substituent [44]. In this regard, it is important to note that the orthotopic U87 model is well known to be characterized by extensive BBB-disruption [45,46], as confirmed by the strong contrast-enhancement observed in the present study. As such, increased permeability of the BBB presumably contributed to tumor uptake of [^{68}Ga]FAPI-04, Al[^{18}F]F-FAPI-42 and, at least to some extent, also 6-[^{18}F]F-FAPI and [^{11}C]RJ1102 in this preclinical model. In line with this assumption, the most pronounced accumulation of both FAP-radioligands in the present study was observed in the contrast-enhancing core region of the intracerebral U87 tumors, while [^{18}F]FET showed a much more diffuse accumulation pattern that appeared to extent beyond the T2-defined tumor border. Importantly however, blocking or displacement with UAMC1110 strongly reduced uptake of 6-[^{18}F]F-FAPI by the intracerebral tumors, indicating that it reflects FAP-specific binding rather than, e.g., passive tracer extravasation due to local BBB impairment. Altogether, these results support the notion that FAPI-PET can be used to detect FAP-positive cerebral lesions and indicate that it may provide complementary information to imaging with amino acid tracers like [^{18}F]FET. However, further preclinical and clinical studies will clearly be required to reliably assess the role of BBB-disruption for FAPI-PET imaging of brain tumors and to identify the most suitable radioligands for different applications (e.g., tumor detection and staging vs. tumor delineation) and/or patient populations (e.g., patients with contrast-enhancing vs. non-enhancing lesions). In addition, pharmacokinetic aspects such as tracer metabolism will need to be investigated in detail in future studies to support clinical translation, particularly since these parameters can differ considerably between rodents and humans, and dedicated toxicity studies will also be required prior to clinical application.

4. Conclusion

In conclusion, our preclinical comparison of three FAP-radioligands prepared by different ^{18}F-labeling methods demonstrates distinct pharmacokinetic profiles and imaging characteristics. Among the evaluated tracers, Al[^{18}F]F-FAPI-42 exhibited the most favorable properties for delineating FAP-positive peripheral tumors, including sustained tumor retention, rapid clearance from plasma and FAP-negative tissues, the lowest hepatobiliary excretion and the highest tumor-to-background ratios. Conversely, 6-[^{18}F]F-FAPI showed higher and more persistent tumor uptake in an orthotopic glioma model, suggesting a potential advantage for brain tumor imaging. In contrast, [^{18}F]AFA-FAPI failed to demonstrate FAP-specific tumor uptake *in vivo*, limiting its suitability for further development. Taken together, these findings provide a rationale for the selection of Al[^{18}F]F-FAPI-42 for peripheral imaging applications and highlight 6-[^{18}F]F-FAPI as a promising candidate for brain tumor imaging. Future studies should investigate pharmacokinetic aspects such as tracer metabolism, assess potential species differences in imaging properties, and include dedicated toxicity studies to further support clinical translation.

5. Materials and methods

5.1. Organic chemistry

5.1.1. General

Unless noted otherwise, all reagents and solvents were purchased from Sigma-Aldrich (Steinheim, Germany), Acros (Fisher Scientific GmbH, Nidderrau, Germany), Alfa Aesar [Thermo Fisher (Kandel) GmbH, Kandel, Germany], BLDPharm (Kaiserslautern, Germany) or Key Organics (Camelford, UK), and used without further purification. Unless noted otherwise, all reactions were carried out with magnetic stirring and, if air or moisture sensitive substrates and/or reagents were used, in flame-dried glassware under argon. Organic extracts were dried over anhydrous Na_2SO_4 or $MgSO_4$. Solutions were concentrated under reduced pressure (1–900 mbar) at 40–50 °C using a rotary evaporator. (*S*)–*N*-[2-(2-Cyano-4,4-difluoropyrrolidin-1-yl)-2-oxoethyl]-6-(1,1-dihydroxyboryl)quinoline-4-carboxamide (**6**) [20], 6-(3-chloropropoxy)quinoline-4-carboxylic acid (**7**) [31], 6-fluoro-2-(methylamino)nicotinic acid (**17**) [32], *N*,*N*,*N*,1-tetramethyl-2,4-dioxo-1,4-dihydro-2*H*-pyrido[2,3-d][1,3]oxazin-7-aminium trifluoromethanesulfonate (**18**•TfOH) [32], and 7-fluoro-1-methyl-2*H*-pyrido[2,3-d][1,3]oxazine-2,4(1*H*)-dione (**19**) [32] were prepared according to the literature.

Proton, carbon and fluorine nuclear magnetic resonance (^{1}H, ^{13}C and ^{19}F NMR) spectra were recorded on a Bruker Avance Neo (400 MHz) spectrometer. Chemical shifts are reported in parts per million (ppm) relative to residual peaks of deuterated solvents. The observed signal multiplicities are characterized as follows: s = singlet, d = doublet, t = triplet, quint = quintet, m = multiplet, dd = doublet of doublets, dddd = doublet of doublets of doublets of doublets, dt = doublet of triplets, tt = triplet of triplets, qd = quartet of doublets, and br = broad. Coupling constants (*J*) are reported in hertz (Hz). Low resolution mass spectra (LRMS) were measured with an MSQ PlusTM mass spectrometer (Thermo Electron Corporation, San Jose, USA). High resolution mass spectra (HRMS) were measured with an LTQ Orbitrap XL (Thermo Fischer Scientific Inc., Bremen, Germany).

5.1.2. Preparation of the precursor for Al[^{18}F]F-FAPI-42

The radiolabeling precursor for Al[^{18}F]F-FAPI-42 was prepared according to the literature [33].

5.1.3. Preparation of the precursor for 6-[^{18}F]F-FAPI

*5.1.3.1. Synthesis of 6-bromoquinoline-4-carboxylic acid 2,3,5,6-tetrafluorophenyl ester (**2**).* EDC•HCl (1.05 g, 5.50 mmol, 1.1 eq.) was added to a suspension of 6-bromoquinoline-4-carboxylic acid (**1**) (1.26 g, 5.00 mmol, 1 eq.) and 2,3,5,6-tetrafluorophenol (872 mg, 5.25 mmol, 1.05 eq.) in CH_2Cl_2 (20 mL) at ambient temperature. The reaction mixture was stirred for 16 h. All volatiles were then removed under reduced pressure and the residue was taken up in a mixture of EtOAc (30 mL) and 10 % citric acid (1 mL). The organic phase was washed with water (3 × 30 mL) and brine (3 × 30 mL), dried, and concentrated under reduced pressure to afford the title compound (1.81 g, 3.76 mmol, 75 % yield based ^{1}H NMR) with 18 % 2,3,5,6-tetrafluorophenol impurity. The raw product was used for the next step without further purification. ^{1}H NMR (400 MHz, $CDCl_3$): δ = 9.15 (d, *J* = 4.5 Hz, 1H), 9.06 (d, *J* = 2.1 Hz, 1H), 8.28 (d, *J* = 4.5, 1H), 8.15 (d, *J* = 9.0 Hz, 1H), 7.94 (d, *J* = 2.1, 9.0 Hz, 1H), 7.14 (tt, *J* = 7.1, 14.7 Hz, 1H). ^{13}C NMR (101 MHz, $CDCl_3$): δ = 161.44, 150.10, 147.91, 146.31 (dd, *J* = 4.4, 249.2 Hz), 140.83 (dd, *J* = 21.8, 250.7 Hz), 134.18, 131.94, 130.37, 129.35, 127.73, 126.11, 124.28, 124.24, 104.15 (t, *J* = 22.8 Hz). ^{19}F NMR (376 MHz, $CDCl_3$): δ = −152.32 (m, 2F), −138.06 (m, 2F). HR-MS-ESI: *m/z* $[M+H]^+$ calculated for $[C_{16}H_7BrF_2NO_2]^+$ = 399.95908, found: 399.95907.

*5.1.3.2. Synthesis of 6-(trimethylstannyl)quinoline-4-carboxylic acid 2,3,5,6-tetrafluorophenyl ester (**3**).* Sn_2Me_6 (0.39 mL, 616 mg, 1.88 mmol, 1.5 eq.) was added to a suspension of LiCl (254 mg, 5.99 mmol, 4.8 eq.) in a solution of **2** (500 mg, 1.25 mmol, 1 eq.) and $Pd(Ph_3P)_4$ (277 mg, 240 µmol, 0.19 eq.) in anhydrous toluene (15 mL) and the reaction mixture was refluxed for 3 h. After the mixture had cooled to ambient temperature, it was filtered through a plug of Celite® and the filter cake was washed with EtOAc. The organic phase was washed with brine (3 × 30 mL), dried, and concentrated under reduced pressure. The residue was purified by flash chromatography (SiO_2, cyclohexane/EtOAc, 19:1) to afford the title compound (343 mg, 0.87 mmol, 55 % yield based on ^{1}H NMR purities of **2** and **3**) as a colorless solid with 15 % 2,3,5,6-tetrafluorphenol impurity. ^{1}H NMR (400 MHz, $CDCl_3$): δ = 9.13 (d, *J* = 4.4 Hz, 1H), 8.95 (s, 1H), 8.22 (m, 2H), 7.99 (dd, *J* = 1.0, 8.2 Hz, 1H) 7.14 (tt, *J* = 7.1, 9.9 Hz, 1H), 0.42 (s, 9H). ^{13}C NMR (101 MHz, $CDCl_3$): δ = 162.07, 149.54, 149.09, 146.33 (dd, *J* = 4.4, 249.2 Hz), 145.83, 140.91 (dd, *J* = 16.0, 252.9 Hz), 137.20, 132.72, 131.35, 128.89, 124.49, 123.24, 104.00 (t, *J* = 22.8 Hz), 29.85, −9.23. ^{19}F NMR (376 MHz, $CDCl_3$): δ = −138.21 to −138.31 (m, 2F), −152.35 to −152.44 (m, 2F). HR-MS-ESI: *m/z* $[M+H]^+$ calculated for $[C_{19}H_{16}F_4NO_2Sn]^+$ = 486.01337, found: 486.01336.

*5.1.3.3. Synthesis of (S)–N-[2-(2-cyano-4,4-difluoropyrrolidin-1-yl)-2-oxoethyl]-6-(trimethylstannyl)quinoline-4-carboxamide (**5**).* A solution of **3** (221 mg, 562 µmol, 1 eq.) in anhydrous CH_2Cl_2 (2 mL) was slowly added to an ice-cold solution of crude (*S*)-[2-(2-cyano-4,4-difluoropyrrolidin-1-yl)-2-oxoethyl]ammonium 4-methylbenzenesulfonate (**4**•TsOH) {prepared by deprotecting the corresponding *N*-Boc-protected amide (213 mg, 589 µmol, 1.05 eq.) with 1.5 eq. TsOH•H_2O in MeCN (4 mL/mmol) for 16 h [9]} and Et_3N (167 µL, 121 mg, 1.20 mmol, 2.1 eq.) in anhydrous CH_2Cl_2 (2 mL), and the reaction mixture was allowed to warm to ambient temperature. After stirring for 3 h, the reaction mixture was diluted with CH_2Cl_2 (5 mL), washed with brine (3 × 5 mL), and dried. The mixture was concentrated under reduced pressure and the residue was purified by flash chromatography (CH_2Cl_2/MeOH, 24:1) to afford the title compound (152 mg, 300 µmol, 53 % yield) as a yellowish solid. ^{1}H NMR (400 MHz, $CDCl_3$): (mixture of rotamers) δ = 8.88 (s, 1H), 8.47–8.35 (m, 1H), 8.10 (d, *J* = 8.2 Hz, 1H), 7.88 (dd, *J* = 0.8, 8,2 Hz, 1H), 7.50 (d, *J* = 4.1 Hz, 1H), 7.14 (s, 1H), 4.98 (t, *J* = 6.5 Hz, 1H), 4.43 (dd, *J* = 5.4, 17.5 Hz, 1H), 4.22 (dd, *J* = 4.3, 17.6 Hz, 1H), 4.07–3.95 (m, 2H), 2.84–2.76 (m, 2H), 0.37 (s, 9H). ^{13}C NMR (101 MHz, $CDCl_3$): δ = 167.49 (d, *J* = 37.2 Hz), 149.44, 148.32, 144.08, 140.65, 137.17, 132.93, 128.43, 125.29, 124.00, 122.78, 118.94, 116.07, 52.21 (t, *J* = 32.5 Hz), 44.42, 42.43, 37.55 (t, *J* = 25.5 Hz), −9.18. ^{19}F NMR (376 MHz, $CDCl_3$): δ = −95.89 to −97.77 (m, 1F), −100.71 to −104.57 (m, 1F). HR-MS-ESI: *m/z* $[M+H]^+$ calculated for $[C_{20}H_{23}F_2N_4O_2Sn]^+$ = 509.08056, found: 509.08026.

5.1.4. Preparation of the precursor for [^{18}F]AFA-FAPI

*5.1.4.1. Synthesis of 6-(3-azidopropoxy)quinoline-4-carboxylic acid (**8**).* 2,6-Lutidine (348 µL, 3.00 mmol, 2 eq.) was added to a solution of 6-(3-chloropropoxy)quinoline-4-carboxylic acid (**7**) (404 mg, 1.53 mmol, 1 eq.), NaN_3 (293 mg, 4.51 mmol, 3 eq.) and NaI (460 mg, 3.07 mmol, 2 eq.) in DMF (5 mL) and the reaction mixture was stirred for 12 h at 60 °C. The mixture was then diluted with H_2O (100 mL), acidified with AcOH (260 µL), and the resulting precipitate was isolated by centrifugation. The solid was dried at 68 °C and 2 mbar for 5 h to afford the title compound (367 mg, 1.35 mmol, 90 % yield) as a yellowish solid. ^{1}H NMR (400 MHz, $[CD_3]_2SO$): δ = 13.75 (br, 1H), 8.87 (t, *J* = 4.4 Hz, 1H), 8.18 (d, *J* = 2.8 Hz, 1H), 8.03 (d, *J* = 9.2 Hz, 1H), 7.94 (d, *J* = 4.4 Hz, 1H), 7.50 (dd, *J* = 2.8, 9.2 Hz, 1H), 4.18 (t, *J* = 6.1 Hz, 2H), 3.57 (t, *J* = 6.7 Hz, 2H), 2.08 (quint, *J* = 6.4 Hz, 2H). ^{13}C NMR (101 MHz, $[CD_3]_2SO$): δ = 167.62, 157.49, 147.62, 144.86, 133.84, 131.24, 125.92, 122.70, 122.16, 104.48, 65.07, 47.74, 28.06. HR-MS-ESI: *m/z* $[M+H]^+$ calculated for $[C_{13}H_{13}N_4O_3]^+$ = 273.09822, found: 273.09844.

*5.1.4.2. Synthesis of 2,3,5,6-tetrafluorophenyl 6-(3-azidopropoxy)quinoline-4-carboxylate (**9**).* A solution of EDC (373 mg, 1.95 mmol, 1.1 eq.) in CH_2Cl_2 (7 mL) was added to a solution of **8** (493 mg, 1.81 mmol, 1 eq.) and 2,3,5,6-tetrafluorophenol (320 mg, 1.93 mmol, 1.1 eq.) in CH_2Cl_2 (4.2 mL) and the mixture was stirred at ambient temperature for 72 h. The solvent was removed under reduced pressure and the residue was taken up in a mixture of 10 % aq. citric acid (10 mL) and EtOAc (20 mL). The organic phase was separated and the aqueous phase was extracted with EtOAc (3 × 10 mL). The combined organic phases were washed with H_2O (3 × 10 mL) and brine (3 × 10 mL), dried, and concentrated under reduced pressure to afford the title compound (696 mg, 1.47 mmol, 81 % yield based on ^{1}H NMR) as a pale-yellow solid, which was used for the next step without further purification. ^{1}H NMR (400 MHz, $CDCl_3$): δ = 8.98 (d, *J* = 4.5 Hz, 1H), 8.23 (d, *J* = 4.6 Hz, 1H), 8.22 (d, *J* = 2.8 Hz, 1H), 8.14 (d, *J* = 9.3 Hz, 1H), 7.48 (dd, *J* = 2.8, 9.3, 1H), 7.11 (tt, *J* = 9.9, 10.6 Hz, 1H), 4.22 (t, *J* = 5.9 Hz, 2H), 3.56 (t, *J* = 6.6 Hz, 2H), 2.14 (quint, *J* = 6.3 Hz, 2H). ^{19}F NMR (376 MHz, $CDCl_3$): δ = −138.23 to −138.32 (m, 2F), −152.38 to −152.47 (m, 2F). HR-MS-ESI: *m/z* $[M+H]^+$ calculated for $[C_{19}H_{13}F_4N_4O_3]^+$ = 421.09183, found: 421.09184.

*5.1.4.3. Synthesis of (S)-6-(3-azidopropoxy)-N-(2-(2-cyano-4,4-difluoropyrrolidin-1-yl)-2-oxoethyl)quinoline-4-carboxamide (**10**).* Et_3N (475 μL, 345 mg, 3.41 mmol, 2.05 eq.) was added to a solution of **4**•TsOH (598 mg, 1.65 mmol, 1.1 eq.) and **9** (696 mg, 1.47 mmol, 1 eq.) in CH_2Cl_2 (8.5 mL), and the reaction mixture was stirred for 24 h. All volatiles were removed under reduced pressure and the residue was taken up in H_2O (12 mL) and EtOAc (25 mL). The organic phase was separated and the aqueous phase was additionally extracted with EtOAc (2 × 15 mL). The combined organic phases were washed with half saturated NH_4Cl (3 × 15 mL), H_2O (3 × 15 mL) and brine (3 × 15 mL), dried, and concentrated under reduced pressure. The crude product thus obtained was recrystallized from isopropanol (15–20 mL) to afford the title compound (542 mg, 1.22 mmol, 83 % yield) as a colorless solid. ^{1}H NMR (400 MHz, CD_3OD): (mixture of rotamers) δ = 8.75 (d, *J* = 4.4 Hz, 1H), 7.98 (d, *J* = 9.3 Hz, 1H), 7.95 (d, *J* = 2.7 Hz, 1H), 7.57 (d, *J* = 4.4 Hz, 1H), 7.48 (dd, *J* = 2.8, 9.2 Hz, 1H), 5.14 (dd, *J* = 3.1, 9.3 Hz, 1H), 4.37–4.28 (m, 4H), 4.26–4.09 (m, 2H), 3.56 (t, *J* = 6.7 Hz, 2H), 2.99–2.76 (m, 2H), 2.14 (quint, *J* = 6.4 Hz, 2H). The signal of N–*H* was not observed. ^{13}C NMR (101 MHz, CD_3OD): δ = 170.74, 169.49, 159.35, 148.10, 145.36, 142.81, 130.90, 127.35, 124.88, 120.37, 118.37, 105.31, 66.81, 52.94 (t, *J* = 32.4 Hz), 45.83 (d, *J* = 5.1 Hz), 42.88, 38.10–37.85 (m), 29.62. ^{19}F NMR (376 MHz, CD_3OD): (mixture of rotamers) δ = −97.08 to −98.60 (m, 1F), −105.38 to −107.86 (m, 1F). HR-MS-ESI: *m/z* $[M+H]^+$ calculated for $[C_{20}H_{20}F_2N_7O_3]^+$ = 444.15902, found: 444.15918.

*5.1.4.4. Synthesis of tert-butyl (S)-[3-({4-[(2-(2-cyano-4,4-difluoropyrrolidin-1-yl)-2-oxoethyl]carbamoyl}quinolin-6-yl)oxy]propyl)carbamate (**11**).* A suspension of 10 % Pd/C (94 mg) in a solution of **10** (413 mg, 931 μmol, 1 eq.) and Boc_2O (305 mg, 1.38 mmol, 1.5 eq.) in MeCN (490 μL) was stirred under H_2 for 3.5 h. The reaction mixture was filtered through a funnel packed with a cotton plug, Na_2SO_4 and Celite® and the filter cake was washed with CH_2Cl_2. The filtrate and washing were combined and all volatiles were removed under reduced pressure to afford the title compound (449 mg, 868 μmol, 93 % yield) as a colorless solid, which was used for the next step without further purification. ^{1}H NMR (400 MHz, CD_3OD): δ = 8.75 (d, *J* = 4.5 Hz, 1H), 7.97 (d, *J* = 9.3 Hz, 1H), 7.89 (d, *J* = 2.4 Hz, 1H), 7.57 (d, *J* = 4.5 Hz, 1H), 7.47 (dd, *J* = 2.7, 9.3 Hz, 1H), 5.16 (dd, *J* = 3.1, 9.3 Hz, 1H), 4.36–4.22 (m, 4H), 4.19–4.07 (m, 2H), 3.30–3.27 (m, 2H), 2.99–2.76 (m, 2H), 2.03 (quint, *J* = 6.6 Hz, 2H), 1.42 (s, 9H). The signals of OCN–*H* and BocN-*H* were not observed. ^{13}C NMR (101 MHz, CD_3OD): δ = 170.71, 169.52, 159.53, 158.53, 148.00, 145.33, 142.66, 130.84, 127.36, 124.96, 120.41, 118.13, 105.21, 79.96, 67.39, 61.53, 52.97 (t, *J* = 32.3 Hz), 45.83 (d, *J* = 5.6 Hz), 42.88, 38.99, 38.13 (t, *J* = 25.4 Hz), 30.49, 28.77. ^{19}F NMR (376 MHz, CD_3OD): δ = −96.59 to −98.84 (m, 1F), −105.33 – 108.16 (m, 1F). HR-MS-ESI: *m/z* $[M+H]^+$ calculated for $[C_{25}H_{30}F_2N_5O_5]^+$ = 518.22095, found: 518.22080.

*5.1.4.5. Synthesis of (S)-6-(3-aminopropoxy)-N-[2-(2-cyano-4,4-difluoropyrrolidin-1-yl)-2-oxoethyl]quinoline-4-carboxamide (**12**•TFA).* **11** (200 mg, 386 μmol, 1 eq.) was added to a mixture of triisopropylsilane (50 μL), H_2O (50 μL) and TFA (1.9 mL), and the reaction mixture was stirred for 15 min. All volatiles were removed under reduced pressure and the residue was taken up in 15 % MeCN (0.1 % TFA). The crude product was purified by preparative HPLC (column: Eurosphere II 100-5 C18A, 250 × 20 mm; eluent: isocratic: 15 % MeCN (0.1 % TFA); flow rate: 18 mL/min; t_R = 7.5–13 min) and lyophilized to afford the title compound (315 mg, >99 % yield) as a yellowish solid. ^{1}H NMR (400 MHz, CD_3OD): δ = 8.96 (d, *J* = 5.0 Hz, 1H), 8.17 (d, *J* = 2.6 Hz, 1H), 8.13 (d, *J* = 9.3 Hz, 1H), 7.85 (d, *J* = 5.0 Hz, 1H), 7.70 (dd, *J* = 2.7, 9.4 Hz, 1H), 5.12 (dd, *J* = 3.4, 9.3 Hz, 1H), 4.47–4.34 (m, 4H), 4.31–4.23 (m, 1H), 4.19–4.09 (m, 1H), 3.21 (t, *J* = 7.4 Hz, 2H), 3.01–2.90 (m, 1H), 2.87–2.77 (m, 1H) 2.27 (quint, *J* = 7.3 Hz, 2H). ^{13}C NMR (101 MHz, CD_3OD): δ = 169.51, 169.12, 162.10, 160.23, 147.59, 145.26, 139.95, 129.87, 127.86, 127.42, 127.38, 126.75, 124.93, 120.81, 118.25, 106.16, 67.51, 52.90 (t, *J* = 32.3 Hz), 45.88 (d, *J* = 5.3 Hz), 42.98, 38.44, 37.97 (t, *J* = 25.3 Hz), 28.06. ^{19}F NMR (376 MHz, CD_3OD): δ = −77.23, −96.68 to −99.39 (m, 1F), −105.09 to −108.15 (m, 1F). LR-MS-ESI: *m/z* $[M+H]^+$ calculated for $[C_{20}H_{22}F_2N_5O_3]^+$ = 418.17, found: 418.11.

5.1.5. Preparation of the reference compound 6-F-FAPI

*5.1.5.1. Synthesis of 6-fluoroquinoline-2,4-dicarboxylic acid (**14**).* Sodium pyruvate (1.98 g, 18.0 mmol, 1.2 eq.) was added to a solution of 5-fluoroindoline-2,3-dione (**13**) (2.48 g, 15.0 mmol, 1 eq.) in 6 M NaOH (30 mL) and the reaction mixture was stirred at 130 °C for 4 h. The resulting precipitate was removed by filtration and washed with 2 M NaOH and EtOH. The combined filtrate and washings were concentrated under reduced pressure and the residue was dried under high vacuum. The off-white solid thus obtained was dissolved in a minimal amount of H_2O and acidified with 37 % HCl (2.1 mL). The resulting precipitate was isolated by filtration, washed with H_2O and dried under high vacuum to afford the title compound (2.43 g, 10.2 mmol, 68 % yield) as an off-white solid, which was used for the next step without further purification. ^{1}H NMR (400 MHz, $[CD_3]_2SO$): δ = 8.56 (m, 2H), 8.32 (dd, *J* = 5.8, 9.3 Hz, 1H), 7.86 (dt, *J* = 2.9, 8.7 Hz, 1H). The signals of CO_2–*H* were not observed. ^{13}C NMR (101 MHz, $[CD_3]_2SO$): δ = 166.13 (d, *J* = 99.7 Hz), 163.19, 160.71, 148.15 (d, *J* = 2.8 Hz), 145.38, 136.12 (d, *J* = 6.0 Hz), 133.73 (d, *J* = 10.1 Hz), 126.79 (d, *J* = 11.7 Hz), 122.73, 121.09 (d, *J* = 26.4 Hz), 109.41 (d, *J* = 25.2 Hz). ^{19}F NMR (376 MHz, $[CD_3]_2SO$): δ = −107.37. LR-MS-ESI: *m/z* $[M+H]^+$ calculated for $[C_{11}H_7FNO_4]^+$ = 236.04, found: 236.07.

*5.1.5.2. Synthesis of 6-fluoroquinoline-4-carboxylic acid (**15**).* A suspension of **14** (1.18 g, 5.01 mmol) in nitrobenzene (10 mL) was refluxed for 50 min before the reaction mixture was diluted with an equal volume of toluene. The resulting precipitate was isolated by filtration, washed with toluene and pentane, and dried under reduced pressure to afford the title compound (866 mg, 4.53 mmol, 90 % yield) as a brownish solid, which was used for the next step without further purification. ^{1}H NMR (400 MHz, $[CD_3]_2SO$): δ = 9.04 (d, *J* = 4.4 Hz, 1H), 8.50 (dd, *J* = 2.9, 11.2 Hz, 1H), 8.20 (dd, *J* = 5.9, 9.3 Hz, 1H), 8.03 (d, *J* = 4.3 Hz, 1H), 7.78 (dt, *J* = 2.9, 13.3 Hz, 1H). The signal of CO_2–*H* was not observed. ^{13}C NMR (101 MHz, $[CD_3]_2SO$): δ = 167.15, 160.67 (d, *J* = 246.3 Hz), 149.98 (d, *J* = 2.6 Hz), 145.89, 134.83 (d, *J* = 5.8 Hz), 132.65 (d, *J* = 9.8 Hz), 125.47 (d, *J* = 11.0 Hz), 123.30, 119.97 (d, *J* = 25.9 Hz), 109.23 (d, *J* = 24.8 Hz).^{19}F NMR (376 MHz, $[CD_3]_2SO$): δ = −110.65. LR-MS-ESI: *m/z* $[M+H]^+$ calculated for $[C_{10}H_7FNO_2]^+$ = 192.05, found:

192.20.

*5.1.5.3. Synthesis of 2,3,5,6-tetrafluorophenyl 6-fluoroquinoline-4-carboxylate (**16**).* EDC•HCl (529 mg, 3.41 mmol, 1.3 eq.) was added (in portions) to an ice-cold suspension of **15** (500 mg, 2.62 mmol, 1 eq.) in a solution of 2,3,5,6-tetrafluorophenol (870 mg, 5.24 mmol, 2 eq.) in CH_2Cl_2 (26 mL). After 10 min, the cooling bath was removed and the reaction mixture was stirred for 16 h before it was diluted with an equal volume of CH_2Cl_2. The resulting mixture was washed with 0.05 M NaOH (3 × 25 mL) and brine (3 × 25 mL), dried, and concentrated under reduced pressure. The residue was purified by flash column chromatography (cyclohexane/EtOAc, 9:1, R_f = 0.17) to afford the title compound (739 mg, 2.18 mmol, 83 % yield) as a colorless solid. ^{1}H NMR (400 MHz, $CDCl_3$): δ = 9.11 (d, *J* = 4.4 Hz, 1H), 8.53 (dd, *J* = 2.8, 10.6 Hz, 1H), 8.26 (m, 2H), 7.62 (dddd, *J* = 2.8, 5.7 Hz, 1H), 7.12 (tt, *J* = 7.1, 9.9 Hz, 1H). ^{13}C NMR (101 MHz, CD_3CN): δ = 163.59, 161.60, 161.09, 149.13 (d, *J* = 2.9 Hz), 147.70–147.42 (m), 146.74, 145.11–144.94 (m), 142.27–141.96 (m), 139.87–139.53 (m), 133.11 (d, *J* = 9.5 Hz), 130.62 (d, *J* = 6.2 Hz), 126.21 (d, *J* = 11.4 Hz), 124.33, 120.91 (d, *J* = 26.1), 109.42 (d, *J* = 25.4 Hz), 104.09 (t, *J* = 22.8 Hz). ^{19}F NMR (376 MHz, $CDCl_3$): δ = −107.80, −138.16 to −138.24 (m, 2F), −152.38 to −152.46 (m, 2F).

5.1.5.4. Synthesis of (S)-6-fluoro-N-[2-(2-cyano-4,4-difluoropyrrolidin-1-yl)-2-oxoethyl]quinoline-4-carboxamide (6-F-FAPI). A solution of **16** (385 mg, 1.13 mmol, 1 eq.) in anhydrous CH_2Cl_2 (3 mL) was slowly added to an ice-cold solution of crude **4**•TFA {prepared by deprotecting the corresponding *N*-Boc-protected amide (344 mg, 1.19 mmol, 1.05 eq.) with 20 % TFA in CH_2Cl_2 (12 mL) for 16 h [30]} and DIPEA (600 µL, 438 mg, 3.39 mmol, 3 eq.) in anhydrous CH_2Cl_2 (9 mL). The cooling bath was removed and the mixture was stirred for 6 h before it was diluted with CH_2Cl_2 (12 mL). The resulting mixture was washed with 10 % citric acid (3 × 15 mL) and brine (3 × 15 mL), dried, and concentrated under reduced pressure. The residue was purified by flash chromatography (CH_2Cl_2/MeOH, 24:1) to afford the title compound (123 mg, 340 µmol, 30 % yield) as an off-white solid. ^{1}H NMR (400 MHz, $CDCl_3$): δ = 8.86 (d, *J* = 3.7 Hz, 1H), 8.12 (dd, *J* = 5.5, 9.2 Hz, 1H), 7.95 (dd, *J* = 2.8, 10.0 Hz, 1H), 7.55–7.49 (m, 2H), 7.39 (s, 1H), 4.99 (dd, *J* = 5.1, 8.0 Hz, 1H), 4.42 (dd, *J* = 5.9, 17.5 Hz, 1H), 4.16 (dd, *J* = 4.2, 17.4 Hz, 1H), 4.12–3.95 (m, 2H), 2.95–2.76 (m, 2H). ^{13}C NMR (101 MHz, $CDCl_3$): δ = 167.35 (d, *J* = 42.6 Hz), 162.59, 160.11, 148.79, 145.44, 140.26, 132.14 (d, *J* = 6.8 Hz), 120.90 (d, *J* = 26.3 Hz), 119.65, 116.22, 109.22 (d, *J* = 24.1 Hz), 52.19 (t, *J* = 32.3 Hz), 44.47, 42.38, 37.43 (t, *J* = 25.5 Hz), 29.84, 27.04. ^{19}F NMR (376 MHz, $CDCl_3$): δ = −95.80 to −97.91 (m, 1F), −100.96 to −104.82 (m, 1F), −109.968. HR-MS-ESI: *m/z* $[M+H]^+$ calculated for $[C_{20}H_{22}F_2N_5O_3]^+$ = 418.16852, found: 418.16863.

5.1.6. Preparation of the reference compound AFA-FAPI

5.1.6.1. Synthesis of (S)–N-[2-(2-cyano-4,4-difluoropyrrolidin-1-yl)-2-oxoethyl]-6-{3-[6-fluoro-2-(methylamino)nicotinamido]propoxy}quinoline-4-carboxamide (AFA-FAPI). A solution of 6-fluoro-2-(methylamino) nicotinic acid (**17**) (5 mg, 29 µmol) in thionyl chloride (1 mL) was stirred at 80 °C for 2 h. All volatiles were removed under reduced pressure, the residue was taken up in toluene (10 mL) and the solution was concentrated under reduced pressure (× 3). A solution of **12**•TFA (12 mg, 29 µmol) and Et_3N (0.3 µL) in CH_2Cl_2 (1 mL) was added to the residue and the resulting mixture was stirred for 1 h. The reaction mixture was diluted with H_2O (10 mL), the resulting emulsion was extracted with CH_2Cl_2 (3 × 10 mL), and the combined organic phases were dried and concentrated under reduced pressure. The residue was purified by flash chromatography (CH_2Cl_2:MeOH = 19:1) to afford the title compound (8 mg, 14 µmol, 48 % yield) as a colorless solid. ^{1}H NMR (400 MHz, CD_3CN): δ = 8.78 (d, *J* = 4.3 Hz, 1H), 8.48 (s, 1H), 7.98 (d, *J* = 9.2 Hz, 1H), 7.86 (t, *J* = 8.2 Hz, 1H), 7.81 (d, *J* = 2.7 Hz, 1H), 7.49 (d, *J* = 4.3 Hz, 1H), 7.41 (dd, *J* = 2.8, 9.2 Hz, 1H), 7.37 (s, 1H), 7.08 (s, 1H), 6.08 (dd, *J* = 2.8, 8.2 Hz, 1H), 4.99 (dd, *J* = 3.3, 9.0 Hz, 1H), 4.27–4.17 (m, 4H), 4.15–4.10 (m, 1H), 4.05–3.95 (m, 1H), 3.53 (qd, *J* = 2.2, 6.4 Hz, 2H), 2.88 (d, *J* = 4.9 Hz, 3H), 2.85–2.70 (m, 2H), 2.11–2.06 (m, 2H). ^{13}C NMR (101 MHz, CD_3CN): δ = 168.87, 168.79, 168.33, 166.49, 164.13, 158.64, 148.44, 145.69, 142.07 (d, *J* = 10.2 Hz), 141.24, 131.99, 127.51–127.46 (m), 126.56, 125.02, 123.60, 120.20, 108.32, 105.19, 93.83 (d, *J* = 39.1 Hz), 67.21, 52.69 (t, *J* = 32.2 Hz), 45.40 (d, *J* = 6.5 Hz), 42.65, 37.74 (t, *J* = 25.0 Hz), 37.36, 29.69, 28.05. ^{19}F NMR (376 MHz, CD_3CN): δ = −65.81, −96.83 to −98.75 (m, 1F), −101.17 to −103.55 (m, 1F). HRMS (ESI): *m/z* calculated for $C_{27}H_{26}F_3N_7O_4^+$: 569.19929, found 569.19881.

5.2. Radiochemistry

5.2.1. General

[^{18}F]Fluoride ([^{18}F]F^-) was produced via the ^{18}O(p,n)^{18}F nuclear reaction by bombardment of enriched [^{18}O]H_2O with 16.5 MeV protons using a BC1710 cyclotron (The Japan Steel Works Ltd., Shinagawa, Japan) at the INM-5 (Forschungszentrum Jülich). All radiosyntheses were carried out in 5 mL Wheaton V-Vials equipped with PTFE-coated wing stir bars. Anhydrous solvents (DMI, *n*BuOH and MeOH, dried over molecular sieves) were purchased from Sigma-Aldrich (Steinheim, Germany). Sep-Pak Accell Plus QMA carbonate plus light cartridges (40 mg sorbent per cartridge) and HLB short cartridges (360 mg sorbent per cartridge) were obtained from Waters GmbH (Eschborn, Germany). Polymeric-based StrataX cartridges (60 mg) were obtained from Phenomenex (Aschaffenburg, Deutschland). Chromabond PS-HCO_3^- Shorty (45 mg sorbent per cartridge) were obtained from Synthra GmbH (Hamburg, Germany).

Analytical radio-HPLC was performed on a HPLC system (Knauer Wissenschaftliche Geräte GmbH, Berlin, Germany) with an Azura P 6.1L pump and an Azura UVD 2.1S UV/Vis detector. For monitoring absorbance at 254 nm and radioactivity, the UV/Vis detector was coupled in series with a Berthold NaI detector, giving a time of delay of 0.1–0.3 min between the corresponding responses (depending on the flow rate). For determination of radiochemical conversions (RCCs), the reaction mixtures were diluted with H_2O (2 mL) or 20 % MeCN (2 mL) and analyzed by radio-HPLC with post-column injection [47]. The RCCs were calculated by comparison of the peak areas of the radiolabeled product and the post-column injection [20]. The identity of radiolabeled products was confirmed by co-injection of the corresponding non-labeled reference compound. Activity yields (AYs) were determined by comparing the initial activity on the QMA cartridge and the activity of the purified radiolabeled product.

Semipreparative HPLC for purification of crude 6-[^{18}F]F-FAPI was performed using a dedicated semipreparative HPLC system consisting of a Merck Hitachi L-6000 pump, a Knauer K-2500 detector, a Rheodyne 6-way valve and a Geiger-Müller counter.

5.2.2. High-performance liquid chromatography (HPLC) conditions

5.2.2.1. Analytical HPLC. 6-[^{18}F]F-FAPI: column: MultoKrom® 100-5 C18, 5 µm, 250 × 4.6 mm (CS-Chromatographie Service GmbH, Langerwehe, Germany); eluent: 30 % MeCN; flow rate: 1.5 mL/min; t_R = 12.2 min.

[^{18}F]AFA-FAPI: column: MultoKrom® 100-5 C18 AQ, 5 µm, 250 × 4.6 mm (CS-Chromatographie Service GmbH, Langerwehe, Germany); eluent: 50 % MeCN; flow rate: 1.0 mL/min; t_R = 8.7 min.

5.2.2.2. Preparative HPLC. 6-[^{18}F]F-FAPI: column: Gemini C18 110A, 5 µm, 250 × 10 mm (Phenomenex Ltd., Aschaffenburg, Germany); eluent: 30 % MeCN; flow rate: 7.1 mL/min; t_R = 12.5–14.5 min.

[^{18}F]AFA-FAPI: column: Synergi Hydro-RP 80A, 10 µm, 250 × 10

mm (Phenomenex Ltd., Aschaffenburg, Germany); eluent: 40 % MeCN; flow rate: 4.7 mL/min; t_R = 20.0–22.5 min.

5.2.2.3. Quality control. 6-[^{18}F]F-FAPI: column: Kinetex EVO C18, 5 μm, 250 × 4.6 mm (Phenomenex Ltd., Aschaffenburg, Germany); eluent: 20 % MeCN, flow rate: 1.5 mL, t_R = 8.42 min.

[^{18}F]AFA-FAPI: column: MultoKrom® 100-5 C18 AQ, 5 μm, 250 × 4.6 mm (CS-Chromatographie Service GmbH, Langerwehe, Germany); eluent: 50 % MeCN; flow rate: 1.0 mL/min; t_R = 8.7 min.

5.2.3. Preparation of Al[^{18}F]F-FAPI-42

Al[^{18}F]F-FAPI-42 was prepared using the Al[^{18}F]F chelation method described by McBride et al. [16] as follows. Aqueous [^{18}F]F$^-$ (0.1–7 GBq) was loaded onto a Sep-Pak Accell Plus QMA carbonate plus light cartridge (preconditioned with 5 mL 0.5 M NaOAc and 10 mL H_2O). The cartridge was washed with H_2O (5 mL) and the [^{18}F]F$^-$ was eluted with 0.05 M sodium acetate buffer (350 μL, pH 4) into a reaction vessel. DMSO (1.4 mL), a solution of FAPI-42 (3.2 mM, 64 nmol) in 0.05 M sodium acetate (20 μL) and a solution of $AlCl_3$•$6H_2O$ (0.01 M, 29 nmol) in 0.05 M sodium acetate (0.3 μL) were then added and the reaction mixture was incubated at 110 °C for 10 min. The crude product solution thus obtained was diluted with H_2O (50 mL) and saturated $NaHCO_3$ (1 mL), and loaded onto a polymer RP cartridge (HLB). The cartridge was washed with H_2O (5 mL) and dried with air (10 mL) before the product was eluted with EtOH (1 mL). The solvent was removed at 600 mbar in a stream of argon, and the residue was taken up in isotonic saline solution.

5.2.4. Preparation of 6-[^{18}F]F-FAPI

Aqueous [^{18}F]F$^-$ (0.1–7 GBq) was loaded (from the male side) onto a QMA cartridge (preconditioned with 1 mL H_2O from the female side). The cartridge was washed (from the male side) with anhydrous MeOH (1 mL) to remove residual H_2O and dried (from the female side) with air (2 × 10 mL). [^{18}F]F$^-$ was then eluted with a solution of Et_4NOTf (1 mg, 4 μmol) in anhydrous MeOH (500 μL) into a V-Vial and the MeOH was evaporated at 60 °C under reduced pressure in a stream of argon. The V-Vial was filled with argon, sealed with a silicon septum and a solution of **5** (5.1 mg, 10 μmol) and Cu(4-PhPy)$_4$(ClO$_4$)$_2$ (8.7 mg, 10 μmol) in DMI (800 μL) was added via a cannula inserted through the septum. The reaction mixture was heated at 90 °C for 10 min, diluted with H_2O (15 mL) and loaded onto a StrataX cartridge. The cartridge was washed with H_2O (5 mL) and the crude radiolabeled product was eluted with MeCN (500 μL). The eluent was diluted with H_2O (1 mL) and purified by preparative HPLC. The product fraction was collected at 12.5–14.5 min. For formulation, the collected fraction was diluted with H_2O (15 mL) and loaded onto a StrataX cartridge. The cartridge was washed with H_2O (5 mL) and dried with air before the radiotracer was eluted with EtOH (500 μL). The solvent was removed at 40 °C under reduced pressure in a stream of argon, and the residue was taken up in 1 % Tween 80 to afford 6-[^{18}F]F-FAPI as a ready-to-inject solution.

5.2.5. Preparation of [^{18}F]AFA-FAPI

The prosthetic group [^{18}F]**19** for radiosynthesis of [^{18}F]AFA-FAPI was prepared as follows: [^{18}F]F$^-$ (0.5–7 GBq) was loaded (from the male side) onto an anion exchange cartridge (PS–HCO_3, 45 mg, preconditioned with 1 mL H_2O from the female side). The cartridge was washed with MeCN (4 mL) and air-dried from the female side. The [^{18}F]F$^-$ was then eluted (from the female to the male side) with a solution of **18**•TfOH (12 mg) in MeCN/*t*BuOH (1.2 mL, 1:2 v/v), followed by flushing of the cartridge with MeCN (1 mL) into the same vial. The resulting solution was diluted with H_2O (19 mL) and loaded onto a SPE cartridge (Oasis® HLB Plus Short), which was washed with 5 % acetone in H_2O (6 mL) and briefly dried in a steam of argon. The prosthetic group [^{18}F]**19** was then eluted with MeCN (1.5 mL) and the mixture was concentrated under reduced pressure at 85 °C to approximately 50–80 μL before a solution of **12**•TFA (5.3 mg, 10 μmol) in 0.2 M borate buffer (pH 8.7)/MeCN (500 μL, 9:1 v/v) was added. The reaction mixture was heated at 35 °C for 15 min. After addition of 0.2 M phosphate buffer (1 mL, pH 7.5), the crude product was purified by semi-preparative HPLC. The product fraction was diluted with H_2O (40 mL) and loaded onto a SPE cartridge (Oasis® HLB Plus Short), which was washed with H_2O (5 mL) before the product was eluted with MeOH (1.5 mL). Subsequent removal of the solvent under reduced pressure in a stream of argon at 60 °C followed by addition of isotonic saline solution afforded [^{18}F]AFA-FAPI as an injectable solution.

5.3. Biological evaluation

5.3.1. Cell cultures

HT1080-WT (ATCC: CCL 121) and HT1080-FAP cells were cultured under normal growth conditions (37 °C and 5 % CO_2) in minimum essential medium GlutaMAX (MEM, Gibco 41090028, Fisher Scientific GmbH, Schwerte, Germany) supplemented with 10 % fetal bovine serum (FBS, Sigma-Aldrich F2442, Merck KGaA, Darmstadt, Germany), 1 % penicillin/streptomycin (Gibco 115140122), 1 % non-essential amino acids (NEAA, Gibco 11140050), 1 % human recombinant insulin (Sigma Aldrich 91077C), and 1 % sodium pyruvate (ThermoFisher 11360070, Fisher Scientific GmbH, Schwerte, Germany). The cells were grown in cell-culture dishes (ThermoFisher 150350, F 100 mm) with 9 mL culture medium and routinely passaged when they had reached 80–90 % confluency (every 4−5 days). For the cellular uptake studies, cells were seeded into 12-well plates (2 × 10^5 cells in 1 mL medium/well) 48 h before the start of the experiments.

5.3.2. Cellular uptake experiments

Two hours prior to the start of experiments, the culture medium was carefully aspirated, the cells were washed with phosphate-buffered saline (PBS, 1 mL, Gibco 10010023), and a dye exclusion test with trypan blue (T 8154, Sigma Aldrich) was performed to determine cell viability and the exact cell count (cell viability was always >95 %). The tracer solutions were prepared in FBS- and amino acid-free Earle's balanced salt solution (EBSS) at a concentration of 150 kBq/mL. PBS was removed from the wells and the tracer solution was added (1 mL/well). The cells were then incubated at 37 °C for 60 min, washed twice with ice-cold PBS (1 mL), trypsinized and harvested. The accumulated radioactivity was measured in an automatic gamma counter (Hidex AMG version 1.4.4, Turku, Finland). Each experiment was conducted at least in triplicate.

5.3.3. Experimental animals

All experiments were carried out in accordance with the EU directive 2010/63/EU for animal experiments and the German Animal Welfare Act (TierSchG, 2006) and were approved by the regional authorities (LANUV NRW; 81-02.04.2020.A348). Twenty-three CB17-SCID mice (11 male, 12 female; Janvier Labs, Le Genest-Saint-Isle, France) and three male Lewis rats (Charles River Laboratories, Sulzfeld, Germany) were used for the *in vivo* experiments. They were housed in groups in individually ventilated cages (Allentown LLC, Allentown, NJ, USA) in a temperature- and humidity-controlled room (20 ± 2 °C, 50–60 % humidity) on a 12:12 h light-dark cycle. Throughout the experiments the animals had *ad libitum* access to water and food.

5.3.4. Subcutaneous HT1080-WT and HT1080-FAP xenograft mouse model

In this model, tracer uptake was compared between tumor xenografts induced by subcutaneous implantation of HT1080-FAP or HT1080-WT cells in T-cell-deficient SCID mice. Mice were between 7 and 8 weeks old and weighed 20–23 g (males) or 16–19 g (females) at the start of the experiments. To promote tumor cell survival and growth, natural killer cell activity was reduced by intraperitoneal injection of 20 μL anti-asialo GM1 rabbit (Fujifilm Wako Chemicals Europe GmbH, Neuss, Germany) diluted with 80 μL 0.9 % NaCl 24 h before tumor inoculation. For tumor inoculation, 2 × 10^6 tumor cells were resuspended in 75 μL culture

medium, mixed with 75 μL Corning Matrigel (Merck KGaA, Darmstadt, Germany), and injected subcutaneously in the right shoulder region. Twelve mice (6 males, 6 females) were inoculated with HT1080-WT cells, and 11 mice (5 males, 6 females) were inoculated with HT1080-FAP cells. PET measurements were performed 10–15 days after tumor implantation.

5.3.5. Subcutaneous DSL allograft rat model

Tumors induced by implantation of DSL-6A/C1 cells are characterized by a pronounced tumor stroma with a high density of FAP-positive CAFs, while the tumor cells themselves should be FAP-negative [35,36]. Rats were between 10 and 14 weeks old and weighed 277–330 g at the start of the experiments. 1×10^7 DSL-6A/C1 rat pancreatic carcinoma cells (CLS Cell Lines Service GmbH, Eppelheim, Germany) were resuspended in 100 μL cell culture medium and injected subcutaneously in the shoulder or hip region. As tumor growth in this model was extremely slow, PET measurements were performed 79–121 days after tumor implantation.

5.3.6. Orthotopic U87 glioma xenograft rat model

For this model, immunodeficient male Rowett Nude Rats (Charles River, Sulzfeld, Germany) weighting 235–304 g were anesthetized with isoflurane (5 % for induction, 3–4 % for maintenance) in O_2/air (3:7) and U87 MG glioma cells (10^5 cells in 1 μL) were stereotactically implanted into the brain. The stereotactic coordinates were 0.5 mm anterior, 2.5 mm lateral and 3 mm ventral from bregma. MRI scans were performed one week after tumor cell implantation to determine the size of the intracranial tumors, and PET measurements followed during the next three days. The MRI measurements were performed under isoflurane anesthesia (5 % for induction, 2.0–2.5 % for maintenance) in an MRI scanner (3T Achieva®, Philips Healthcare, Best, The Netherlands) in combination with an 8 Channel Volumetric Rat Array (Rapid Biomedical GmbH, Rimpar, Germany). The MRI protocol included horizontal and transverse T2-weighted sliced spin echo sequences to localize the tumor and a coronal T1-weighted sliced gradient echo sequence for contrast-enhanced measurements. The spin echo acquisition included the following parameters: TR = 14540 ms, TE = 30 ms, FA = 90°, FOV = 60 × 60 × 60 mm^3 at 0.3 × 0.3 mm^2 acquired and 0.19 × 0.19 mm^2 reconstructed in-plane resolution, slice thickness 1 mm, TSE factor 19, halfscan 0.6, 2 averages. The T1-weighted scans were acquired prior to and after i.v. contrast agent administration (Clariscan, GE Healthcare, 0.5 mmol/mL, 0.2 mL/kg body weight) with: TR = 230 ms, TE = 4.7 ms, FA = 60°, FOV = 60 × 60 × 22 mm^3 at 0.3 × 0.3 mm^2 acquired and 0.27 × 0.27 mm^2 reconstructed in-plane resolution, slice thickness 1 mm, slice gap: 0.1 mm, CS-SENSE factor 2, 4 averages.

5.3.7. PET measurements

Mice and rats were anesthetized with isoflurane (5 % for induction, 2 % for maintenance) in O_2/air (3:7), and a catheter for tracer injection was inserted into the lateral tail vein. They were placed on an animal holder (mice: double mouse holder from Medres, Cologne, Germany; rats: single rat holder from Minerve, Esternay, France) and fixed with a tooth bar in a respiratory mask. Body temperature was maintained at 37 °C by warming the animal bed. Eyes were protected from drying with Bepanthen eye and nose ointment (Bayer AG, Leverkusen, Germany). Respiratory rate was monitored and maintained at around 40–60 breaths per minute by adjusting the isoflurane concentration. PET scans were conducted in list mode using a Focus 220 micro PET scanner (CTI-Siemens, Erlangen, Germany) with a resolution at the centre of field of view of 1.4 mm. Data acquisition started with intravenous tracer injection and ended after 120 min. For blocking experiments (n = 2) in the U87 glioma model, 5 mg/kg UAMC1110 were injected together with 6-[^{18}F]F-FAPI. For displacement (n = 1), 5 mg/kg UAMC1110 was injected (i.v.) 60 min after 6-[^{18}F]F-FAPI injection. Emission scans were followed by a 10 min transmission scan using a ^{57}Co point source for attenuation correction. After the scan, the catheter was removed and the animals were allowed to recover in their home cages. Data were histogrammed in two ways: 4 × 30 min frames for visual display and 28 frames (2 × 1 min, 2 × 2 min, 6 × 4 min, 18 × 5 min) for time-activity curves. Full 3D rebinning was followed by an iterative OSEM3D/MAP reconstruction algorithm with attenuation and decay correction. The resulting voxel sizes were 0.47 mm × 0.47 mm × 0.80 mm. All further analyses were performed with the software VINCI 5.21 (Max Planck Institute for Metabolism Research, Cologne, Germany). Standardized uptake values based on body weight (SUV_{bw}) were determined according to the following equation: SUV_{bw} = radioactivity [Bq/g] × body weight [g]/injected dose [Bq]. For determination of plasma half-lives, time-activity curves in plasma were extracted using an ellipsoid VOI (26 voxels) placed in the lumen of the left ventricle of the heart. The resulting plasma clearance curves were fitted with a bi-exponential decay model using the following equation: $Y(t) = A \cdot e^{-k_1 t} + B \cdot e^{-k_2 t}$, where A and B are amplitudes of the fast and slow components, and k_1 and k_2 are the corresponding rate constants. The distribution half-life ($t_{1/2,fast}$) and elimination half-life ($t_{1/2,slow}$) were calculated separately as: $t_{1/2,i} = \frac{ln\,2}{k_i}, i = 1, 2$. Curve fitting was performed in Python (SciPy curve_fit) using weighted nonlinear least-squares regression. Initial parameter estimates were chosen based on the first data point and expected kinetic ranges (fast phase ~0.5–1 min^{-1}, slow phase ~0.01–0.05 min^{-1}). The plateau parameter was fixed at 0 to improve stability, as complete plasma clearance was expected.

CRediT authorship contribution statement

Chris Hoffmann: Writing – review & editing, Writing – original draft, Visualization, Investigation, Formal analysis. **Benedikt Gröner:** Writing – original draft, Investigation, Formal analysis. **Victor Bahutski:** Investigation, Formal analysis. **Heike Endepols:** Writing – review & editing, Writing – original draft, Visualization, Supervision, Investigation, Formal analysis, Conceptualization. **Johannes Lindemeyer:** Investigation, Formal analysis. **Sven Saniternik:** Investigation, Formal analysis. **Birte Drewes:** Investigation, Formal analysis. **Marco Timmer:** Investigation, Formal analysis. **Otari Gokhadze:** Investigation, Formal analysis. **Melanie Brugger:** Investigation, Formal analysis. **Felix Neumaier:** Writing – review & editing, Writing – original draft, Visualization, Formal analysis. **Bernd Neumaier:** Writing – review & editing, Supervision, Project administration, Funding acquisition, Conceptualization. **Boris D. Zlatopolskiy:** Writing – review & editing, Writing – original draft, Visualization, Supervision, Investigation, Funding acquisition, Formal analysis, Conceptualization.

Ethics approval and consent to participate

All experiments were carried out in accordance with the EU directive 2010/63/EU for animal experiments and the German Animal Welfare Act (TierSchG, 2006) and were approved by the regional authorities (LANUV NRW; reference number: 81-02.04.2020.A348).

Consent for publication

Not applicable.

Availability of data and materials

The datasets used and analyzed during the current study are available from the corresponding author on reasonable request.

Funding

This work was supported by Deutsche Forschungsgemeinschaft (DFG; grant number ZL 65/4-1), the Shota Rustaveli National Science Foundation of Georgia (SRNSFG; grant number JFZ–II–22-074), and the

Excellent Research Support Program, University of Cologne (UoC) Forum 2023 (Multimodal Preclinical Imaging Platform University Cologne [MUPIC]).

Declaration of competing interest

The authors declare that they have no known competing financial interests or personal relationships that could have appeared to influence the work reported in this paper.

Acknowledgements

PET measurements were carried out at the Central Core Facility "Experimental and Preclinical Imaging Cologne (EPIC)", supported by the Medical Faculty of the University of Cologne.

List of abbreviations

6-[^{18}F]F-FAPI – (*S*)–*N*-[2-(2-cyanopyrrolidin-1-yl)-2-oxoethyl]-6-[^{18}F]fluoroquinoline-4-carboxamide
[^{18}F]AFA – 1-alkylamino-7-[^{18}F]fluoro-8-azaisatoic anhydride
[^{18}F]AFA-FAPI – 6-{[^{18}F]fluoro-2-(methylamino)nicotinamido} propoxy-UAMC1110
[^{18}F]F$^-$ – [^{18}F]fluoride
[^{18}F]FDG – [^{18}F]fluorodeoxyglucose
[^{18}F]FET – *O*-(2-[^{18}F]fluoroethyl)-L-tyrosine
Al[^{18}F]F – aluminum [^{18}F]fluoride
A_m – molar activity
AY – activity yield
BBB – blood-brain barrier
CA – contrast agent
CAFs – cancer-associated fibroblasts
EBSS – Earle's balanced salt solution
FAP – fibroblast activation protein
FAPI – fibroblast activation protein inhibitor
FBS – fetal bovine serum
HPLC – high-performance liquid chromatography
HRMS – high resolution mass spectra
HT1080-FAP – FAP-transfected HT1080 human fibrosarcoma cells
HT1080-WT – non-transfected HT1080 human fibrosarcoma cells
LRMS – low resolution mass spectra
NMR – nuclear magnetic resonance
PBS – phosphate-buffered saline
PET – positron emission tomography
PG – prosthetic group
ppm – parts per million
RCC – radiochemical conversion
RCP – radiochemical purity
rt – room temperature
SPE – solid phase extraction
SUV_{bw} – standardized uptake value based on body weight
TAC – time-activity curve
TBR – tumor-to-background ratio
TFA – trifluoroacetate
TfO$^-$ – trifluoromethanesulfonate
Tfp – 2,3,5,6-tetrafluorophenyl
TsO$^-$ – tosylate

Appendix A. Supplementary data

Supplementary data to this article can be found online at https://doi.org/10.1016/j.ejmech.2025.118103.

Data availability

Data will be made available on request.

References

[1] A.A. Fitzgerald, L.M. Weiner, The role of fibroblast activation protein in health and malignancy, Cancer Metastasis Rev. 39 (2020) 783–803. Available from: https://link.springer.com/10.1007/s10555-020-09909-3.
[2] E.J. Hamson, F.M. Keane, S. Tholen, O. Schilling, M.D. Gorrell, Understanding fibroblast activation protein (FAP): substrates, activities, expression and targeting for cancer therapy, PROTEOMICS - Clin. Appl. 8 (2014) 454–463. Available from: https://onlinelibrary.wiley.com/doi/10.1002/prca.201300095.
[3] M. Sollini, M. Kirienko, F. Gelardi, F. Fiz, N. Gozzi, A. Chiti, State-of-the-art of FAPI-PET imaging: a systematic review and meta-analysis, Eur. J. Nucl. Med. Mol. Imaging. 48 (2021) 4396–4414. Available from: https://link.springer.com/10.1007/s00259-021-05475-0.
[4] R. Huang, Y. Pu, S. Huang, C. Yang, F. Yang, Y. Pu, et al., FAPI-PET/CT in cancer imaging: a potential novel molecule of the century, Front. Oncol. 12 (2022) 854658. Available from: https://www.frontiersin.org/articles/10.3389/fonc.2022.854658/full.
[5] T. Lindner, F.L. Giesel, C. Kratochwil, S.E. Serfling, Radioligands targeting fibroblast activation protein (FAP), Cancers (Basel) 13 (2021) 5744. Available from: https://www.mdpi.com/2072-6694/13/22/5744.
[6] F.L. Giesel, C. Kratochwil, J. Schlittenhardt, K. Dendl, M. Eiber, F. Staudinger, et al., Head-to-head intra-individual comparison of biodistribution and tumor uptake of ^{68}Ga-FAPI and ^{18}F-FDG PET/CT in cancer patients, Eur. J. Nucl. Med. Mol. Imaging. 48 (2021) 4377–4385. Available from: https://link.springer.com/10.1007/s00259-021-05307-1.
[7] S. Ballal, M.P. Yadav, E.S. Moon, V.S. Kramer, F. Roesch, S. Kumari, et al., Biodistribution, pharmacokinetics, dosimetry of [^{68}Ga]Ga-DOTA.SA.FAPi, and the head-to-head comparison with [^{18}F]F-FDG PET/CT in patients with various cancers, Eur. J. Nucl. Med. Mol. Imaging. 48 (2021) 1915–1931. Available from: https://link.springer.com/10.1007/s00259-020-05132-y.
[8] K. Jansen, L. Heirbaut, J.D. Cheng, J. Joossens, O. Ryabtsova, P. Cos, et al., Selective inhibitors of fibroblast activation protein (FAP) with a (4-quinolinoyl)-glycyl-2-cyanopyrrolidine scaffold, ACS Med. Chem. Lett. 4 (2013) 491–496. Available from: https://pubs.acs.org/doi/10.1021/ml300410d.
[9] K. Jansen, L. Heirbaut, R. Verkerk, J.D. Cheng, J. Joossens, P. Cos, et al., Extended structure–activity relationship and pharmacokinetic investigation of (4-quinolinoyl)glycyl-2-cyanopyrrolidine inhibitors of fibroblast activation protein (FAP), J. Med. Chem. 57 (2014) 3053–3074. Available from: https://pubs.acs.org/doi/10.1021/jm500031w.
[10] A. Loktev, T. Lindner, W. Mier, J. Debus, A. Altmann, D. Jäger, et al., A tumor-imaging method targeting cancer-associated fibroblasts, J. Nucl. Med. 59 (2018) 1423–1429. Available from: http://jnm.snmjournals.org/lookup/doi/10.2967/jnumed.118.210435.
[11] T. Lindner, A. Loktev, A. Altmann, F. Giesel, C. Kratochwil, J. Debus, et al., Development of quinoline-based theranostic ligands for the targeting of fibroblast activation protein, J. Nucl. Med. 59 (2018) 1415–1422. Available from: http://jnm.snmjournals.org/lookup/doi/10.2967/jnumed.118.210443.
[12] A. Loktev, T. Lindner, E.-M. Burger, A. Altmann, F. Giesel, C. Kratochwil, et al., Development of fibroblast activation protein–targeted radiotracers with improved tumor retention, J. Nucl. Med. 60 (2019) 1421–1429. Available from: http://jnm.snmjournals.org/lookup/doi/10.2967/jnumed.118.224469.
[13] A. Sanchez-Crespo, Comparison of gallium-68 and fluorine-18 imaging characteristics in positron emission tomography, Appl. Radiat. Isot. 76 (2013) 55–62. Available from: https://linkinghub.elsevier.com/retrieve/pii/S0969804312004708.
[14] K. Hu, J. Li, L. Wang, Y. Huang, L. Li, S. Ye, et al., Preclinical evaluation and pilot clinical study of [^{18}F]AlF-labeled FAPI-tracer for PET imaging of cancer associated fibroblasts, Acta Pharm. Sin. B 12 (2022) 867–875. Available from: https://linkinghub.elsevier.com/retrieve/pii/S2211383521003932.
[15] T. Lindner, A. Altmann, F. Giesel, C. Kratochwil, C. Kleist, S. Krämer, et al., ^{18}F-Labeled tracers targeting fibroblast activation protein, EJNMMI Radiopharm. Chem. 6 (2021) 26. Available from: https://ejnmmipharmchem.springeropen.com/articles/10.1186/s41181-021-00144-x.
[16] W.J. McBride, R.M. Sharkey, H. Karacay, C.A. D'Souza, E.A. Rossi, P. Laverman, et al., A novel method of ^{18}F radiolabeling for PET, J. Nucl. Med. 50 (2009) 991–998. Available from: http://jnm.snmjournals.org/lookup/doi/10.2967/jnumed.108.060418.
[17] F.L. Giesel, S. Adeberg, M. Syed, T. Lindner, L.D. Jiménez-Franco, E. Mavriopoulou, et al., FAPI-74 PET/CT using either ^{18}F-AlF or cold-kit ^{68}Ga labeling: biodistribution, radiation dosimetry, and tumor delineation in lung cancer patients, J. Nucl. Med. 62 (2021) 201–207. Available from: http://jnm.snmjournals.org/lookup/doi/10.2967/jnumed.120.245084.
[18] K. Hu, L. Wang, H. Wu, S. Huang, Y. Tian, Q. Wang, et al., [^{18}F]FAPI-42 PET imaging in cancer patients: optimal acquisition time, biodistribution, and comparison with [^{68}Ga]Ga-FAPI-04, Eur. J. Nucl. Med. Mol. Imaging. 49 (2022) 2833–2843. Available from: https://link.springer.com/10.1007/s00259-021-05646-z.
[19] J. Toms, J. Kogler, S. Maschauer, C. Daniel, C. Schmidkonz, T. Kuwert, et al., Targeting fibroblast activation protein: radiosynthesis and preclinical evaluation of an ^{18}F-Labeled FAP inhibitor, J. Nucl. Med. 61 (2020) 1806–1813. Available from: http://jnm.snmjournals.org/lookup/doi/10.2967/jnumed.120.242958.
[20] N. Walter, J. Bertram, B. Drewes, V. Bahutski, M. Timmer, M.B. Schütz, et al., Convenient PET-tracer production via SuFEx ^{18}F-fluorination of nanomolar precursor amounts, Eur. J. Med. Chem. 237 (2022) 114383. Available from: https://linkinghub.elsevier.com/retrieve/pii/S0223523422002859.

[21] N. Zhang, F. Pan, L. Pan, W. Diao, F. Su, R. Huang, et al., Synthesis, radiolabeling, and evaluation of a (4-quinolinoyl)glycyl-2-cyanopyrrolidine analogue for fibroblast activation protein (FAP) PET imaging, Front. Bioeng. Biotechnol. 11 (2023) 1167329. Available from: https://www.frontiersin.org/articles/10.3389/fbioe.2023.1167329/full.

[22] Z. Yu, Y. Huang, H. Chen, Z. Jiang, C. Li, Y. Xie, et al., Design, synthesis, and evaluation of ^{18}F-Labeled tracers targeting fibroblast activation protein for brain imaging, ACS Pharmacol. Transl. Sci. 6 (2023) 1745–1757. Available from: https://pubs.acs.org/doi/10.1021/acsptsci.3c00187.

[23] M. Röhrich, A. Loktev, A.K. Wefers, A. Altmann, D. Paech, S. Adeberg, et al., IDH-wildtype glioblastomas and grade III/IV IDH-mutant gliomas show elevated tracer uptake in fibroblast activation protein–specific PET/CT, Eur. J. Nucl. Med. Mol. Imaging. 46 (2019) 2569–2580. Available from: http://link.springer.com/10.1007/s00259-019-04444-y.

[24] P. Windisch, M. Röhrich, S. Regnery, E. Tonndorf-Martini, T. Held, K. Lang, et al., Fibroblast activation protein (FAP) specific PET for advanced target volume delineation in glioblastoma, Radiother. Oncol. 150 (2020) 159–163. Available from: https://linkinghub.elsevier.com/retrieve/pii/S0167814020303650.

[25] F.L. Giesel, C.P. Heussel, T. Lindner, M. Röhrich, H. Rathke, H.-U. Kauczor, et al., FAPI-PET/CT improves staging in a lung cancer patient with cerebral metastasis, Eur. J. Nucl. Med. Mol. Imaging. 46 (2019) 1754–1755. Available from: http://link.springer.com/10.1007/s00259-019-04346-z.

[26] W. Fu, L. Liu, H. Liu, Z. Zhou, Y. Chen, Increased FAPI uptake in brain metastasis from lung cancer on ^{68}Ga-FAPI PET/CT, Clin. Nucl. Med. 46 (2021) e1–e2. Available from: https://journals.lww.com/10.1097/RLU.0000000000003357.

[27] H. Kömek, C. Can, Y. Güzel, Z. Oruç, C. Gündoğan, Ö.A. Yildirim, et al., ^{68}Ga-FAPI-04 PET/CT, a new step in breast cancer imaging: a comparative pilot study with the ^{18}F-FDG PET/CT, Ann. Nucl. Med. 35 (2021) 744–752. Available from: https://link.springer.com/10.1007/s12149-021-01616-5.

[28] Y. Wei, J. Zheng, L. Ma, X. Liu, S. Xu, S. Wang, et al., [^{18}F]AlF-NOTA-FAPI-04: FAP-targeting specificity, biodistribution, and PET/CT imaging of various cancers, Eur. J. Nucl. Med. Mol. Imaging. 49 (2022) 2761–2773. Available from: https://link.springer.com/10.1007/s00259-022-05758-0.

[29] Y. Yao, X. Tan, W. Yin, Y. Kou, X. Wang, X. Jiang, et al., Performance of ^{18}F-FAPI PET/CT in assessing glioblastoma before radiotherapy: a pilot study, BMC Med. Imaging. 22 (2022) 226. Available from: https://bmcmedimaging.biomedcentral.com/articles/10.1186/s12880-022-00952-w.

[30] K. Jansen, I. De Meester, L. Heirbaut, J.D. Cheng, J. Joossens, K. Augusyns, et al., Novel FAP inhibitors,, WO 2013/107820 A1,, https://lens.org/071-367-093-519-975, 2013.

[31] U. Haberkorn, A. Loktev, T. Lindner, W. Mier, D. Jäger, N. Halama, FAP inhibitor,, WO 2019/154859 A1,, https://lens.org/164-137-892-630-491, 2019.

[32] B. Gröner, M. Willmann, L. Donnerstag, E.A. Urusova, F. Neumaier, S. Humpert, et al., 7-[^{18}F]Fluoro-8-azaisatoic anhydrides: versatile prosthetic groups for the preparation of PET tracers, J. Med. Chem. 66 (2023) 12629–12644. Available from: https://pubs.acs.org/doi/10.1021/acs.jmedchem.3c01310.

[33] U. Haberkorn, A. Loktev, T. Lindner, W. Mier, F. Giesel, C. Kratochwil, FAP inhibitor,, WO 2019/154886 A1,, https://lens.org/182-135-720-730-959, 2019.

[34] C. Hoffmann, N. Kolks, D. Smets, A. Haseloer, B. Gröner, E.A. Urusova, et al., Next generation copper mediators for the efficient production of ^{18}F-Labeled aromatics, Chem. Eur J. 29 (2023) e202202965. Available from: https://onlinelibrary.wiley.com/doi/10.1002/chem.202202965.

[35] O.S. Pettengill, R.A. Faris, R.H. Bell, E.T. Kuhlmann, D.S. Longnecker, Derivation of ductlike cell lines from a transplantable acinar cell carcinoma of the rat pancreas, Am. J. Pathol. 143 (1993) 292–303. Available from: http://www.ncbi.nlm.nih.gov/pubmed/8391218.

[36] H.G. Hotz, H.A. Reber, B. Hotz, T. Foitzik, H.J. Buhr, G. Cortina, et al., An improved clinical model of orthotopic pancreatic cancer in immunocompetent lewis rats, Pancreas 22 (2001) 113–121. Available from: http://journals.lww.com/00006676-200103000-00002.

[37] A. Verger, A. Kas, J. Darcourt, E. Guedj, PET imaging in neuro-oncology: an update and overview of a rapidly growing area, Cancers (Basel) 14 (2022) 1103. Available from: https://www.mdpi.com/2072-6694/14/5/1103.

[38] E.E. Parent, A. Sharma, M. Jain, Amino acid PET imaging of glioma, Curr. Radiol. Rep. 7 (2019) 14. Available from: http://link.springer.com/10.1007/s40134-019-0324-x.

[39] P. Busek, E. Balaziova, I. Matrasova, M. Hilser, R. Tomas, M. Syrucek, et al., Fibroblast activation protein alpha is expressed by transformed and stromal cells and is associated with mesenchymal features in glioblastoma, Tumor Biol. 37 (2016) 13961–13971. Available from: http://link.springer.com/10.1007/s13277-016-5274-9.

[40] C.D. Arvanitis, G.B. Ferraro, R.K. Jain, The blood–brain barrier and blood–tumour barrier in brain tumours and metastases, Nat. Rev. Cancer 20 (2020) 26–41. Available from: https://www.nature.com/articles/s41568-019-0205-x.

[41] J.N. Sarkaria, L.S. Hu, I.F. Parney, D.H. Pafundi, D.H. Brinkmann, N.N. Laack, et al., Is the blood–brain barrier really disrupted in all glioblastomas? A critical assessment of existing clinical data, Neuro Oncol. 20 (2018) 184–191. Available from: http://academic.oup.com/neuro-oncology/article/20/2/184/4107399.

[42] M. Djekidel, R. Alsadi, M. Abi Akl, O. Bouhali, J. O'Doherty, Tumor microenvironment and fibroblast activation protein inhibitor (FAPI) PET: developments toward brain imaging, Front. Nucl. Med. 3 (2023) 1183471. Available from: https://www.frontiersin.org/articles/10.3389/fnume.2023.1183471/full.

[43] M. Röhrich, R. Floca, L. Loi, S. Adeberg, P. Windisch, F.L. Giesel, et al., FAP-specific PET signaling shows a moderately positive correlation with relative CBV and no correlation with ADC in 13 IDH wildtype glioblastomas, Eur. J. Radiol. 127 (2020) 109021. Available from: https://linkinghub.elsevier.com/retrieve/pii/S0720048X20302102.

[44] C. Wang, Z. Hu, F. Ding, H. Zhao, F. Du, C. Lv, et al., Radiosynthesis and first preclinical evaluation of the novel ^{11}C-Labeled FAP inhibitor ^{11}C-FAPI: a comparative study of ^{11}C-FAPIs and (^{68}Ga) Ga-DOTA-FAPI-04 in a High–FAP-Expression mouse model, Front. Chem. 10 (2022) 939160. Available from: https://www.frontiersin.org/articles/10.3389/fchem.2022.939160/full.

[45] C. Brighi, L. Reid, L.A. Genovesi, M. Kojic, A. Millar, Z. Bruce, et al., Comparative study of preclinical mouse models of high-grade glioma for nanomedicine research: the importance of reproducing blood-brain barrier heterogeneity, Theranostics 10 (2020) 6361–6371. Available from: http://www.thno.org/v10p6361.htm.

[46] J.A. Schulz, L.T. Rodgers, R.J. Kryscio, A.M.S. Hartz, B. Bauer, Characterization and comparison of human glioblastoma models, BMC Cancer 22 (2022) 844. Available from: https://bmccancer.biomedcentral.com/articles/10.1186/s12885-022-09910-9.

[47] S. Humpert, C. Hoffmann, F. Neumaier, B.D. Zlatopolskiy, B. Neumaier, Validation of analytical HPLC with post-column injection as a method for rapid and precise quantification of radiochemical yields, J. Chromatogr. B. 1228 (2023) 123847. Available from: https://linkinghub.elsevier.com/retrieve/pii/S157002322300257X.